Article:
Su, Y., Li, X., Zhang, C. et al. (2025) Carbon accumulation rate peaks at 1,000-m elevation in tropical planted and regrowth forests. One Earth, 8 (1). 101147. ISSN: 2590-3330

https://doi.org/10.1016/j.oneear.2024.11.001

Carbon accumulation rate peaks at 1000m elevation in tropical planted and regrowth forests

Yongxian Su[1,2,*], Xueyan Li[2,#], Chaoqun Zhang[1,3,#], Wenting Yan[1,3,#], Philippe Ciais[4], Susan Cook-Patton[5], Oliver L. Phillips[6], Jiali Shang[7], Alessandro Cescatti[8], Jing-Ming Chen[9], Jane Liu[9], Jerome Chave[10], Christopher E Doughty[11], Viola Heinrich[12], Feng Tian[13], Yiqi Luo[14], Yi Liu[15], Zhen Yu[16], Dalei Hao[17], Shengli Tao[18], Yongguang Zhang[19], Zhenzhong Zeng[20], Raffaele Lafortezza[21], Yuanyuan Huang[22], Lei Fan[23], Xuhui Wang[18], Yuanwei Qin[24], Qinwei Ran[18], Kai Yan[25], Xiaoping Liu[3], Liyang Liu[4], Yuemin Yue[26], Jiashun Ren[1,3], Wenping Yuan[3], Xiuzhi Chen[3]

1. State Key Laboratory of Urban and Regional Ecology, Research Center for Eco-Environmental Sciences, Chinese Academy of Sciences, Beijing, China;

2. Guangzhou Institute of Geography, Guangdong Academy of Sciences, Guangzhou, China

3. Guangdong Province Data Center of Terrestrial and Marine Ecosystems Carbon Cycle, School of Atmospheric Sciences, Sun Yat-sen University, Zhuhai, China;

4. Laboratoire des Sciences du Climat et de l'Environnement, IPSL, CEA-CNRS-UVSQ, Université Paris-Saclay, Gif sur Yvette, France;

5. The Nature Conservancy, Arlington, VA, USA;

6. School of Geography, University of Leeds, Leeds, UK;

7. Ottawa Research and Development Centre, Agriculture and Agri-Food Canada, Ottawa, Ontario, Canada;

8. European Commission, Joint Research Centre, Ispra, Italy;

9. Department of Geography and Planning, University of Toronto, Ontario, Canada;

10. CNRS, Université Toulouse 3 Paul Sabatier, IRD, UMR 5174 Evolution et Diversité Biologique (EDB), Toulouse, France;

11. School of Informatics, Computing, and Cyber Systems, Northern Arizona University, Flagstaff, AZ, USA;

12. Helmholtz GFZ German Research Centre for Geoscience, Section 1.4 Remote Sensing and Geoinformatics, Potsdam, Germany

13. Hubei Key Laboratory of Quantitative Remote Sensing of Land and Atmosphere, School of Remote Sensing and Information Engineering, Wuhan University, Wuhan 430079, China;
14. School of Integrative Plant Science, Cornell University, Ithaca, NY, USA;
15. Institute of Atmospheric Physics, Chinese Academy of Sciences, Beijing, China;
16. Institute of Ecology and School of Applied Meteorology, Nanjing University of Information Science & Technology, Nanjing, China;
17. Atmospheric Sciences and Global Change Division, Pacific Northwest National Laboratory, Richland, WA, USA;
18. Institute of Ecology, Sino-French Institute for Earth System Science, College of Urban and Environmental Sciences, and Key Laboratory for Earth Surface Processes of the Ministry of Education, Peking University, Beijing 100871, China
19. International Institute for Earth System Sciences, Nanjing University, Nanjing, China;
20. School of Environmental Science and Engineering, Southern University of Science and Technology, Shenzhen, China;
21. Department of Soil, Plant and Food Sciences, University of Bari "A. Moro", Bari, Italy;
22. Key Laboratory of Ecosystem Network Observation and Modeling, Institute of Geographic Sciences and Natural Resources Research, Chinese Academy of Sciences, Beijing, China;
23. School of Geographical Sciences, Southwest University, Chongqing, China;
24. Department of Microbiology and Plant Biology, Center for Earth Observation and Modeling, University of Oklahoma, Norman, OK, USA;
25. Center for GeoData and Analysis, State Key Laboratory of Remote Sensing Science, Faculty of Geographical Science, Beijing Normal University, Beijing 100875, China;
26. Key Laboratory for Agro-ecological Processes in Subtropical Region, Institute of Subtropical Agriculture, Chinese Academy of Sciences, Changsha, China
Corresponding authors: Y. Su (yxsu@rcees.ac.cn)

Lead Contact author: Y. Su (yxsu@rcees.ac.cn)

Keywords: Tropical forests; Biomass carbon accumulation; Planted forests; Natural growth forests; Elevational pattern

Abstract

The Planted and Regrowth forests (TPRFs) are one most low-cost component for recovering biomass-stored carbon in the tropics. Nevertheless, challenges persist in pinpointing which elevational ranges exhibit the largest carbon accumulation rate (γ_{rapid}), due to the highly inconsistent previous assessments. This prevents the selection of optimal locations for implementing large-scale reforestation in the tropics. Here we proposed a refined approach that used a carbon accumulation threshold (< 80% of the maximum value) to quantify γ_{rapid} in TPRFs at various elevations. We find that γ_{rapid} increases with elevations from 300 m to 1000 m and declines at elevations >1000 m. TPRFs at elevation ~1000 m exhibit three times more γ_{rapid} than lowland TPRFs. This optimal elevation, highly dependent of background temperatures, varies slightly but significantly across different mountains. These findings provide guidelines for policymakers to determine the optimal elevations from regional to continental scales when implementing reforestation initiatives in the tropics.

Introduction

Tropical forests account for approximately 40-50% of global forest carbon sink[1, 2]. Nevertheless, tropical forests are under threat from ongoing deforestation, with high risks of flipping into a net carbon source[3, 4]. Thus, it is essential to regenerate tree cover pan-tropically, either in areas where forests have historically existed (termed 'reforestation') or where they have never existed before (termed 'afforestation')[5]. Forest cover can either return naturally following land abandonment (natural regrowth forests) or intentionally (planted forests). These have been recognized as one of the most low-cost approaches for recovering biomass-stored carbon in the tropics[6-8].

Nonetheless, a comprehensive analysis on the optimal locations for implementing afforestation and reforestation is still lacking[9]. One key aspect to be considered when implementing afforestation and reforestation for climate mitigation is the carbon accumulation rate[10, 11], a factor varying significantly with elevation. Recent studies have attempted to use *in situ* data[12-16] and high-resolution European Space Agency Climate

Change Initiative (ESA-CCI) aboveground biomass (AGB) datasets to quantify the carbon accumulation rates in forests[10, 17-18]. Among them, some studies highlighted the existence of elevational patterns of biomass carbon in tropical forests, although these patterns vary across studies[19-28]. For instance, some found that tropical biomass carbon declined[19-22] or increased[23, 24] monotonically with elevation, while others indicated U-shaped[25-27] or inverted U-shaped[28] elevational patterns. Overall, we still lack a large-scale understanding of how the carbon accumulation rate varies with elevation in the tropics[29, 30]. This is partly due to the fact that trees at different elevations were often at diverse growth stages, with various carbon accumulation rates related to age, i.e., higher in young than in mature forests[31, 32]. Current studies commonly used a stand age window to determine the temporal position along a Chapman–Richards curve[10] for calculating the carbon accumulation rate[9]. However, the rates of carbon accumulation, as estimated from different stand ages, may lead to contradictory assessments, complicating the determination of their elevational patterns on large scales[33]. It is thus necessary to develop approaches that enable comparing forest biomass carbon accumulation rates at the same growth stage across various elevations.

Here we conducted a pan-tropical analysis of the growth trajectories in the Tropical Planted and Natural regrowth forests (TPRFs) (**Figure 1a**). We proposed a refined approach that used a carbon accumulation threshold (< 80% of the maximum value), to quantify the biomass carbon accumulation rate (γ_{rapid}) of TPRFs regarding their rapid growth phase prior to reaching maturity[34], which is the most important stage during tree's lifespan for accumulating biomass carbon. Our analysis reveals a robust and consistently increasing trend in γ_{rapid} at elevations from 300 m to 1000 m, but a subsequently declining trend when elevations > 1000 m. This optimal elevation also varies across mountains with different background temperatures. Our findings can help guiding reforestation initiatives at the optimal elevations from regional to continental scales in the tropics.

Results

Overview of experimental procedures

Instead of using fixed stand ages, here we use the time at which a certain biomass carbon threshold is reached, to estimate γ_{rapid} across varying elevations. As such, the rapid growth age is defined as those before the year when the biomass carbon reaches 80% of its peak value predicted by the Chapman–Richards model[35], specifically the median biomass carbon of old-growth forests with stand age $\geqslant$100 years within each elevation bin (**Figures S1 and S2**). It coincides with the year at which the growth rate experiences a slowdown breakpoint in the relationship with stand age as stand age increases (see **Experimental Procedure** for details, **Figure S3**). Since different datasets have different strengths and weaknesses; *in-situ* data provide high precision but are limited by their spatial and temporal consistency, while satellite-based data typically offer comprehensive coverage but often contain noise in specific areas. On the other hand, model-based data are global in scope but generally have low resolution and lack consistent validation; thus, we integrated four independent forest biomass and carbon datasets to conduct a constraint assessment of elevation-driven variations in γ_{rapid}: (i) **Dataset 1**: *in situ* observations of the total forest biomass (aboveground and belowground), sourced from published literature compilation[9] and the Smithsonian Institution's Global Forest Carbon database[36] (hereafter $\boldsymbol{\gamma_{rapid}^{GFC}}$); (ii) **Dataset 2**: the total forest biomass carbon derived from the satellite-based 100 m resolution single-year product of ESA-CCI AGB[17] ($\boldsymbol{\gamma_{rapid}^{ESA-CCI}}$); (iii) **Dataset 3**: a 0.1° resolution time-series dataset of carbon stock in total live woody biomass, generated through machine-learning (ML)[37] ($\boldsymbol{\gamma_{rapid}^{ML}}$); and (iv) **Dataset 4**: a ~0.07° resolution time-series dataset of net ecosystem productivity (NEP) simulations obtained from the BEPS (Boreal Ecosystem Productivity Simulator)[38] model ($\boldsymbol{\gamma_{rapid}^{BEPS}}$). We also examined the elevational gradient of carbon accumulation rates by comparing the rates with the growth rate of tree height ($\boldsymbol{\gamma_{rapid}^{GEDI}}$), which was obtained independently from 30 m resolution spaceborne LiDAR observations in 2019 by the Global Ecosystem Dynamics Investigation (GEDI)[39]

148 **(Dataset 5)**. Corresponding stand age data and methods used to quantify γ_{rapid} for
149 each carbon dataset were introduced in **Table 1**. Here, we focused exclusively on
150 forests with over 80% of the area covered by newly planted or naturally regrown
151 trees, situated at low-to-mid elevations up to 2000 m above mean sea level (a.m.s.l.)
152 as most afforestation and reforestation are implemented below this elevation[40].
153
154 ***Continental-scale elevational pattern of*** $\boldsymbol{\gamma_{rapid}}$
155 The average growth rate of TPRFs before 80% of the peak biomass, γ_{rapid},
156 estimated from the four biomass carbon datasets (**Table 1, Figure 1a**) all shows no
157 significant elevation-dependence at lowlands (elevation < 300m), whereas there is a
158 strong effect of elevation above 300m **(Figures 1b-1e)**. Generally, mountainous γ_{rapid}^{GFC}
159 increases substantially (slope = 0.036±0.0005 MgC·ha^{-1}yr^{-1} m^{-1}; P < 0.05) from
160 1.41±0.26 MgC·ha^{-1}yr^{-1} at an elevation of 290±50 m (P<0.001) to 4.65±0.71 MgC·ha^{-1}yr^{-1} at 1090±50 m (P < 0.001) and then declines as elevation exceeds approximately
162 1090±50 m (slope = -0.0072±0.0059 MgC·ha^{-1}yr^{-1}m^{-1}, P=0.35). TPRFs at elevations
163 of 1000 m demonstrate the highest γ_{rapid}^{GFC}, accumulating approximately 3.0 times more
164 biomass carbon per year than that of their lowland counterparts (**Figure 1b**). Notably,
165 this "inverted U" elevational trend is consistently observed in $\gamma_{rapid}^{ESA-CCI}$ (**Figure 1c**),
166 in which $\gamma_{rapid}^{ESA-CCI}$ is 2.19±0.16 MgC·ha^{-1}yr^{-1} at 290±50 m (P < 0.001), 3.94±0.41
167 MgC·ha^{-1}yr^{-1} at 1090±50 m (P < 0.001) and falls to 2.19±0.17 MgC·ha^{-1}yr^{-1} at
168 1970±50 m (P < 0.001). Similar patterns are also evident in γ_{rapid}^{ML} (**Figure 1d**) and
169 γ_{rapid}^{BEPS} (**Figure 1e**), although their average magnitudes and corresponding slopes of the
170 increasing elevational trends are much smaller due to the coarse spatial resolutions of
171 the datasets. The elevation dependence is also supported by the growth rate of tree
172 height (γ_{rapid}^{GEDI}) calculated from an independent, widely-used spaceborne LiDAR tree
173 height dataset (**Figure 1f**).
174 We then compared the elevational pattern of γ_{rapid} between the natural regrowth

and planted forests, between the broadleaved and needle-leaved forests, between the forests located in south- and north facing slopes of mountains, and among different tree genera[44] (**Figure 2**). While the overall elevational patterns in γ_{rapid} are still valid, γ_{rapid} of planted forests increases more rapidly with elevation than that of natural regrowth forests in areas below 1000 m; conversely, in areas above 1000 m, natural regrowth forests show more pronounced negative elevational gradients in their growth rate than planted forests (**Figures 2a, 2d and 2g**). The elevational patterns of γ_{rapid} also differ between the broadleaved and needle-leaved forests. Generally, the broadleaved forests have a higher value of mean γ_{rapid} compared with needle-leaved forests, while the elevational gradients of γ_{rapid} are more pronounced in needle-leaved forests than in broadleaved forests (**Figures 2b, 2e and 2h**). We also found consistent elevational patterns of γ_{rapid} from 300 m to 1000 m in some specific tree genera (**Figure S4**). However, their elevational patterns above 1000 m were unclear due to the limited availability of biomass carbon data above 1000 m. Additionally, there are no significant differences in the elevational patterns of γ_{rapid} between south- and north facing slopes (**Figures 2g-2i**). This finding aligns with the results observed by Maass et al. (2002)[45], Mendez-Toribio (2016)[46], and Madhumali et al. (2023)[47], which reported insignificant differences in tree height between south- and north- facing slopes in tropical mountains.

Notably, the above-mentioned elevational patterns of γ_{rapid} cannot be correctly represented by approaches that necessitate assuming a specific stand age to estimate the carbon accumulation rate, which theoretically varies with the assumed stand age (**Figure 3a**). This is due to the fact that, in the real world, at elevations below 1000 m, the sensitivities of carbon accumulation to elevation are mostly positive and increase with stand age in a range from 1 to approximately 20-25 years (black points, **Figure 3c**). Conversely, as stands age is beyond 30 years, the sensitivities decline and become negative. In contrast, at elevations above 1000 m, the sensitivities of carbon accumulation to elevation are mostly negative and decrease with stand age rapidly after the age of 20 years (black triangle, **Figure 3c**). This implies that TPRFs at elevations

of 1000m exhibit the fastest growth between 20 and 25 years, while TPRFs at elevations < 300m or > 1000m achieve peak growth rates beyond 30 years **(Figure 3c**). In addition, we also found that planted forests achieves their peak growth rates earlier (about 20 years) than natural regrowth forests (about 25 years) **(Figure S5**).

We then explored various stand age windows (i.e., from zero to 20, 24, 28 and 32 years of age) for calculating the biomass average accumulation rate along the Chapman–Richards curve to assess the reliability of stand-age-based approaches (**Figure 3d**), in comparison with using different peak biomass thresholds (i.e., from zero to the time of reaching 70%, 80% and 90% of the maximum value). We found that the biomass carbon accumulation rate exhibits a positive relationship with elevation below 1000 m when selecting stand age thresholds of less than 20 and 25 years (red and yellow fitted lines, **Figure 3d**) and becomes independent of elevation when 28 years are used as the threshold (green fitted line, **Figure 3d**). However, shifting into negative trends occurs when opting for a threshold stand age of 32 years (dark blue fitted line, **Figure 3d**). These results suggest that using a fixed stand age threshold to compare the carbon accumulation rate may lead to various elevational patterns that are difficult to be interpreted.

In contrast, γ_{rapid} estimated using different stand age at which a biomass threshold is reached (**Figure 3b**), identified by 70%, 80% and 90% of the maximum biomass on the Chapman–Richards curve, show consistent elevational patterns (**Figure 3f**). We further verified that stand ages (age_{rapid}) with rapid accumulation rate identified using our biomass carbon thresholds are comparable with the observed stand age at which a breakpoint is found in the relationship between the carbon accumulation rate and sand age (**Figure S3**). Results indicate that the estimated age_{rapid} using 80% carbon accumulation window coincide the best with those estimated from observed data (**Figure 3e**). Overall, γ_{rapid} is insensitive to various moving windows lengths and enables a reasonable comparison across elevations, ensuring the robustness of our findings.

Climate drivers of elevational gradients in γ_{rapid}

The carbon accumulation rate is determined by two gross carbon fluxes: gross primary production (GPP) and total respiration (TER)[50, 51]. Over a decadal time span, nearly all augmented carbon goes into stand biomass, while the dynamics of soil carbon are much slower[52, 53]. Consequently, we used BEPS-simulated NEP (GPP minus TER, **Dataset 4**)[38], which exhibits a more comparable magnitude with the carbon accumulation rate than net primary production (NPP) (**Figure S7**), as a proxy to explore the intra-annual variation of their elevation dependence on a monthly time scale.

Our analyses indicate that at elevations < 1000 m, GPP and TER both show positive correlations with elevation, but their intra-annual sensitivities differ greatly (**Figure 4a**). Low-land forests experience stronger high-temperature stress (> 24°C) from April to September due to the negative elevational gradients in temperature (**Figure 4c**), resulting in a sharper decrease in GPP than in TER (**Figure 4g**). This discrepancy causes greater negative sensitivities of GPP to elevation compared with TER (**Figure 4i**), thereby leading to positive elevational gradients in NEP from April to September (**Figure 4a**). Furthermore, the decrease in VPD with elevation (**Figure S8a**), emerges as the second crucial factor in co-driving the increasing trend in GPP with elevation. Large VPD serves as a valuable proxy for atmospheric dryness and often imposes significant constrains on GPP in tropical forests[54-58], thus highlighting the impact of elevational on NEP during periods of high-temperature stress (**Figure 4i**). During the high-precipitation months from April to September (**Figure 4e**), elevation-associated variations in precipitation exert a nearly equivalent inhibitory effect on both GPP and TER (**Figures 4h and 4i**). Consequently, the asynchronous elevational sensitivities of GPP and TER to temperature primarily contribute to the positive response of NEP (orange curve) to elevation (< 1000 m).

At elevations above 1000 m, forests grow in moderate temperature conditions (average monthly MAT< 24°C) (**Figure 4d**). In this condition, NEP shows insignificant elevational gradients from April to November (**Figure 4b**), due to the consistent elevational sensitivities of GPP and TER to temperature (< 24°C) (**Figure 4g**). During

the low-precipitation months from December to March, elevation-associated variations in precipitation (**Figure 4f**) exerts divergent impacts on GPP and TER (**Figure 4h**). This discrepancy results in a negative elevational pattern of GPP and a positive elevational pattern of TER (**Figures 4b and 4j**), thereby leading to negative elevational gradients in NEP from December to March (**Figure 4b**). The asynchronous elevational sensitivities of GPP and TER to precipitation primarily contribute to the negative response of NEP at elevations > 1000 m.

Overall, the pronounced elevational patterns in MAT, VPD and precipitation primarily drive the seasonally-dependent but divergent sensitivities of GPP and TER to elevation. These impacts contribute to the increasing elevational trend of γ_{rapid}^{BEPS} at elevations < 1000m and the decreasing elevational trend of γ_{rapid}^{BEPS} at elevations > 1000 m. In contrast, soil moisture (SM) (**Figures S8c-S8d**) and total photosynthetically active radiation (PAR) (**Figures S8e-S8f**) exhibit lower sensitivity to elevation and play less important roles (**Figures 4i-4j**).

Variations at individual mountains

We further examined the elevation patterns of γ_{rapid}^{BEPS} and corresponding driving mechanisms across four mountainous areas: the Sierra Madre del Sur mountain in North America (SMS), the Ethiopian Highlands mountain in Africa (EH), the Serra do Espinhaço mountain in South America (SE), and the Eastern Ghats mountain in Asia (EG) (**Figure 5a**). γ_{rapid}^{BEPS} in individual mountains shows an increase with elevation in low-to-mid elevation, followed by a decline as elevation continues to increase (**Figures 5b-5e**), consistent with the results for entire tropical mountain regions (**Figure 1**). Mechanism analyses also support that the positive elevational gradient of γ_{rapid} is mainly attributed to the asymmetrical response of GPP and TER to temperatures (**Figures S9 and 5i-5l**); while the negative elevational gradient of γ_{rapid} is due to the divergent response of GPP and TER to precipitation (**Figures S9 and 5m-5p**).

However, the optimal elevations where show the γ_{rapid}^{BEPS} peak varies across

different mountains. Among the four studied mountains, the Eastern Ghats mountain experiences the highest mean temperature (average monthly TMF = 26.61°C) (**Figure 5f**) and thus has a highest optimal elevation (1390 m), corresponding to the places with greatest γ_{rapid}^{BEPS} (**Figure 5e**). This results in the smallest elevational sensitivity in γ_{rapid}^{BEPS} (**Figure 5h**). Conversely, the Serra do Espinhaço mountain has the lowest mean temperature (average monthly TMF = 23.67°C) (**Figure 5f**) and shows the lowest optimal elevation (900 m) (**Figure 5d**). This leads to the sharpest elevational trend in γ_{rapid}^{BEPS} (**Figure 5h**). Overall, the optimal elevations with highest γ_{rapid}^{BEPS} in the four mountains are ranked as follows: Eastern Ghats (1390 m) > Ethiopian Highlands (1200 m) > Sierra Madre del Sur mountain (1000 m) > Serra do Espinhaço (900 m) (**Figure 5g**); and in the opposite, the elevational sensitivities of γ_{rapid}^{BEPS} are ranked as: Serra do Espinhaço > Sierra Madre del Sur mountain > Ethiopian Highlands > Eastern Ghats (**Figure 5h**).

Discussion

Afforestation and reforestation stand out as pivotal land-based actions for mitigating climate change, especially in the context of diminishing net gains from CO_2 fertilization and increasingly negative impacts on tree growth from climate warming[59]. Tropical mountain forests exhibit a large potential for carbon accumulation[29, 60]. However, the expansion of a new agricultural frontier has caused significant tree cover loss in tropical mountain forests during the 21st century[61, 62]. Thus, tropical mountains have emerged as a region with significant potential for implementing reforestation and afforestation efforts for future climate mitigation[40].

Challenges persist in pinpointing optimal elevations for afforestation and reforestation in the tropics[59]. Previous field studies generally presented inconsistent elevational patterns of carbon accumulations rate[19, 20, 22-26, 30, 63]. Studies, mainly focusing on the net carbon dynamics of mature forests, observed a monotonically decreasing trend of biomass carbon with elevation at a large elevational range (0-5000

m)[22, 25, 30]. Other studies that accounted for both young and mature forests found that biomass carbon accumulation rate show an inverted U-shaped[28] curve along increasing elevation with a transition at approximately 1600 m[20, 63]. Stand age differences across elevations likely introduce considerable uncertainties when comparing carbon accumulation rates across various elevations.

Notably, such stand-age-associated discrepancy across elevations raises an important issue — how to choose an appropriate time period along a Chapman–Richards curve for quantifying the carbon accumulation rate at different elevations[9]. For instance, young secondary forests (< 40 years old) can accumulate 11 to 20 times more biomass carbon than the mature forests[31, 32]. Studies using the same stand age window for different elevations to estimate the carbon accumulation rate[9] may bring uncertainties when comparing the carbon accumulation rate at various elevations[10], as the stand age varies greatly at different elevations in the real world[64]. This provides explainations for previous studies that have observed diverse elevational patterns of the carbon accumulation rate[9, 25, 30]. Thus, previous studies mostly did not accounted for the uncertainties introduced by different stand age and likely compared the carbon accumulation rate of forests at different growth stages[63]. This can be reflected by the analysis regarding the relationship between biomass carbon accumulation rate and elevations, using 24, 28, and 32 years of age as thresholds, which showed positive, insignificant, and ultimately negative trends, respectively (**Figure 3d**).

To reduce such uncertainties from stand age, we proposed a refined approach that used a carbon accumulation threshold (< 80% of the maximum value) rather than the stand age window to define the analysis time period. This novel approach enables comparing the carbon accumulation rates during the rapid growth periods in both low- and mid-elevation TPRFs (**Figure 3b**), revealing a robust, consistent and positive elevational gradient in γ_{rapid} within elevation below 1000 m and conversely a negative elevational gradient in γ_{rapid} within elevation above 1000 m. (**Figures 1 and 3f**). This discovery helps to reconcile the diverging elevational trends that were observed in previous studies[60, 63, 65] and provides a benchmark for comparing the

biomass carbon accumulation rate (γ_{rapid}) of forests across elevations.

We further found that seasonal variations in temperature and atmospheric dryness play key roles in the positive elevational gradient of γ_{rapid} at elevations < 1000 m. This is probably attributed to the decreases of high-temperature stress[66] and atmospheric dryness constraint[54] with elevation (**Figures 4c and S8a**). This finding is consistent with previous analyses, which found the greatest threat of high-temperature to the biomass carbon accumulation rate in lowland TPRFs[67, 68]. In contrast, TPRFs above 1000m often live in less hot temperatures[69] and thus γ_{rapid} exhibits less impact from high-temperature stress. Conversely, precipitation becomes the most important climatic limiter, as elevations above 1000 m generally have small rainfall[25]. The constraint on GPP from low precipitation, which also causes an increase in TER, is typically severe from December to March, resulting in a negative elevational pattern of γ_{rapid} at elevations above 1000m. Therefore, elevations of around 1000 m likely encounter less high temperature and water stress (**Figures 4c-4f**), making these regions optimal for potential reforestation efforts aimed at climate mitigation.

Notably, the elevational pattern of γ_{rapid} may be further exacerbated by ongoing climate warming[70, 71], as future extreme high temperatures and atmospheric drying could impose more substantial limitations on carbon accumulation rates in the lowlands[72, 73]. With the declining strength of carbon sinks in lowland tropical forests[68], the importance of montane systems for carbon management may be increasing in the future[74]. Climate change may also bring various impacts on the elevational gradients in carbon accumulation between the planted and natural growth forests, and between the broadleaved and needle-leaved forests, as well as in different mountains, due to their diverse climatic sensitivities[13, 14, 18]. Worthy of noting is that disturbances from human activities[10, 18] also decrease with elevation (**Figure S10b**) and may also contribute to the increasing elevational trend of γ_{rapid} in TPRFs (**Figures S10c and S10d**).

In summary, using multiple data streams, as well as modelling and mapping approaches, our analysis reveals a robust and consistently increasing trend in γ_{rapid} at elevations between 300 m and 1000 m, but a subsequently declining trend when

elevations > 1000 m. Thus, 1000 m shows to be the optimal elevation for accumulating biomass carbon in TPRFs, while this threshold varies slightly across different mountains. Our findings underscores the importance of incorporating elevation as a global factor when estimating biomass carbon sinks, and when considering suitable areas for reforestation and afforestation, addressing both scientific understanding and policy considerations.

EXPERIMENTAL PROCEDURES

Methods

General summary

In order to conduct a constraint assessment of elevation-driven variations in the biomass carbon accumulation rate in the rapid growth stages (γ_{rapid}), we firstly collected five independent forest biomass, carbon flux, and height datasets. (i) **Dataset 1**: *in situ* observations of total forest biomass (aboveground and belowground) from published literature compilation[9] and the Smithsonian Institution's Global Forest Carbon database (ForC)[36]; (ii) **Dataset 2**: total forest aboveground biomass carbon derived from the satellite-based 100 m resolution single-year product of European Space Agency Climate Change Initiative (ESA CCI) aboveground biomass (AGB)[17]; (iii) **Dataset 3**: a 0.1° resolution time-series dataset of carbon stock in total live woody biomass, generated through machine-learning (ML)[37]; (iv) **Dataset 4**: a 0.072727° resolution time-series of net ecosystem productivity (NEP) simulations obtained from the BEPS (Biosphere-atmosphere Exchange Process Simulator)[38] model; and (v) **Dataset 5**: a 30 m resolution tree height dataset from spaceborne LiDAR observations in 2019 by the Global Ecosystem Dynamics Investigation (GEDI)[39].

While **Dataset 1** includes information on stand ages, **Datasets 2- 5** do not provide this information. Consequently, we needed to supplement **Datasets 2- 5** with stand age data from other sources before proceeding with the subsequent analysis. For ESA-CCI AGB data (**Datasets 2**) and GEDI tree height data (**Datasets 5**), we utilized the 30 m resolution satellite-based tropical moist forest cover change dataset (TMF)[41] to identify

natural regrowth (TRF) pixels where a conversion from deforested land to forest occurred, termed "Secondary Forest" in the TMF dataset (see more detail later in methods). The consecutive years during which the land remained forest-covered were then used to estimate the stand age in years[18] for these TRF pixels. We also employed a satellite-based global plantation years dataset[42] with a resolution of 30 m to identify planted forest (TPF) pixels and their corresponding planting years. For the 0.1° resolution time-series machine-learning live woody biomass data provided by Xu et al. (2021)[37] **(Dataset 3)** and the 0.072727° resolution time-series BEPS-modeled NEP data **(Dataset 4),** we identified TPRF pixels where non-forests converted to forested lands based on the 0.05° resolution MODIS MCD12C1 landcover products[43]. And then, we supplemented the elevation data for these five independent datasets with Shuttle Radar Topography Mission (SRTM) DEM data[75] extracted from global digital elevation model (DEM) maps.

After supplementing the information on stand age and elevation, we analyzed the γ_{rapid} of TPRFs across the elevation gradient based on these five biomass-related datasets. It is essential to highlight that we applied a space-for-time analogy with the Chapman–Richards curve[10] (**Equation 1**) to estimate γ_{rapid}^{GFC}, $\gamma_{rapid}^{ESA-CCI}$ and γ_{rapid}^{GEDI} at an elevation bin of 100 m and a moving window step of 80 m. Previous studies commonly used a stand age window to determine the temporal position along a Chapman–Richards curve for calculating the carbon accumulation rate[9]. Nevertheless, the rates of carbon accumulation, as estimated from different stand age windows, vary largely (**Figure 3a**). Here, we use a carbon accumulation window approach to estimate the biomass carbon accumulation rate of TPFs during their rapid growth phase (γ_{rapid}), across varying elevations (**Figure 3b**). The rapid growth stand age is defined as the time before the maturity year when the biomass carbon reaches 80% of its peak value predicted by the Chapman–Richards model, specifically the median biomass carbon of old-growth forests with stand age $\geqslant$100 years within each elevation bin. The grid cells corresponding to old-growth forests ($\geqslant$100 years of age) were identified based on stand age information sourced from a global database of forest carbon provided by Anderson-

Teixeira et al[36]. Subsequently, the γ_{rapid} is calculated as the slope of the linear regression fit between live biomass carbon and forest stand age of TPRFs before reaching the defined maturity age (inset in **Figures 1b-1c, 1f; and S1-S2**). It implies that this approach enables comparisons of the biomass carbon accumulation rate in TPRFs during their rapid growth stage, reducing uncertainties arising from differences in stand age across various elevations.

$$Y_t = A(1 - e^{-kt})^c \pm \varepsilon; \text{A, } k \text{ and } c > 0 \quad (1)$$

Where Y_t refers to the biomass carbon at age t; A is the median biomass carbon of old-growth forests with stand age $\geqslant$100 years within each elevation bin; k is a growth rate coefficient of Y_t as a function of age; c is a coefficient that determines the shape of the growth curve; and ε is an error term.

While the γ_{rapid}^{GFC}, $\gamma_{rapid}^{ESA-CCI}$ and γ_{rapid}^{GEDI} are estimated using the space-for-time method, the γ_{rapid}^{ML} and γ_{rapid}^{BEPS} are obtained using time series methods. Specifically, γ_{rapid}^{ML} is estimated as the slope of the fitted linear regression fit between annual live biomass carbon and stand age over the entire time series period for each TPRF (inset in **Figure 1d**), since their stand ages typically span less than 20 years. On the other hand, γ_{rapid}^{BEPS} is calculated as the mean NEP for each TPRF over the same period (**Figure 1e**).

In addition to examining the entire tropical mountain zones, we analyzed the changes in γ_{rapid} with elevation across four specific mountains: the Sierra Madre del Sur in North America (SMS), the Ethiopian Highlands in Africa (EH), the Serra do Espinhaço in South America (SE), and the Eastern Ghats in Asia (EG), using time-series BEPS-modeled net ecosystem productivity (NEP) data (**Figures 5b-e**). Furthermore, we conducted a comprehensive assessment to explore the driving mechanisms behind the elevational gradients in γ_{rapid}, both across the entire tropical regions **(Figure 4)** and among the individual mountains (**Figure 5**).

The overall technical roadmap is shown in **Figure S11** and detailed estimation steps for each dataset are described in the subsequent sections.

462

463 ***Estimation of the biomass carbon accumulation rate based on in situ forest biomass***
464 ***data (Dataset 1) using the space-for-time analogy***

465 We used a global forest biomass carbon dataset that provided field measurements
466 of plant biomass carbon (including both above- and below-ground biomass carbon) (in
467 MgC ha^{-1}), stand age (in years), elevation (in meters), pre-disturbed land cover
468 information and plant establishment method (e.g. natural regrowth or planted)[9, 36]. In
469 cases where records lacked elevation information, we supplemented the elevation data
470 from Shuttle Radar Topography Mission (SRTM) DEM data[75]. Finally, the dataset
471 comprised 2,693 aboveground carbon estimates within tropical regions, originating
472 from 518 distinct sites and encompassing data from 164 studies (**Figure 1a**).

473 Due to the limited availability of time-series observations for each site (mostly
474 spanning over one or two years)[9], we employed a space-for-time analogy to estimate
475 the carbon accumulation rate. In contrast to time-series analysis, which quantifies
476 changes in plant carbon over time at each site, the space-for-time analogy estimates an
477 average carbon accumulation rate across all sites within a specific elevation range.
478 **Figure 1b** was produced at an elevation bin of 100 m and a moving window step of 80
479 m. We conducted additional analyses with various combinations of elevation bins and
480 moving window steps to assess the robustness of the results (**Figure S12**).

481 In addition, using the plant establishment and pre-disturbed land cover information
482 recorded in this database, along with 500 m resolution MODIS MCD12Q1 v061 land
483 cover data[43] and 90 m resolution DEM data[75], we further conducted a comparative
484 analysis of the elevational patterns of γ_{rapid}^{GFC} between natural regrowth and planted
485 forests (**Figure 2a**), between broadleaved and needle-leaved forests (**Figure 2b**),
486 between south- and north-facing slopes of mountains (**Figure 2c**), and different land
487 use types before afforestation, reforestation or both (**Figure S13**).

488

489 ***Estimation of the biomass carbon accumulation rate based on the 100 m resolution***
490 ***total biomass carbon derived from the ESA-CCI aboveground biomass (AGB)***

product (Dataset 2) using the space-for-time analogy

We first obtained the aboveground biomass (AGB) records for 2018 from the 100 m resolution ESA-CCI product[17], which used elevation data to reduce errors arising from the differences in radar backscatter between slopes facing the radar and those facing away. We then used the root-to-shoot ratio developed from field measurements to estimate the below-ground biomass (BGB) from the ESA-CCI AGB data[37, 76]. Subsequently, biomass carbon was estimated from the sum of AGB and BGB by multiplying by a constant coefficient (0.49)[76, 77]. It is important to acknowledge potential uncertainties in these estimates, considering that AGB and BGB may exhibit distinct elevational patterns globally[75, 78-81].

To estimate the $\gamma_{rapid}^{ESA-CCI}$ for natural regrowth forests (TRFs), we utilized the 30 m resolution satellite-based tropical moist forest cover change dataset (TMF)[41] to identify TRF pixels. This dataset tracked the extent and alterations of tropical moist forests over the past three decades[41] and characterized the degraded forests and secondary forests at a spatial resolution of 30 m and a yearly temporal resolution, generated from Landsat data spanning from 1982 to 2019. Degraded forests, in this dataset, were defined as tree-covered pixels for which disturbances were visible for a short time period (between 3 months and 2.5 years maximum), whereas secondary forests were defined as pixels with natural regrowth vegetation after an absence of tree cover for more than 2.5 years[18]. In this study, we only selected the secondary forests for TRF analysis. Furthermore, we also removed the oil palm plantations from the TMF secondary forests following the methodology of Heinrich et al.[18]. Stand age for TRFs was estimated as duration since the most recent disturbance event for any recovering forest pixel in tropical moist forests, based on the annual number of detected disturbances in the TMF dataset. Subsequently, we superimposed the 30m resolution stand age map onto the 100 m resolution total biomass carbon map derived from ESA-CCI AGB production, calculating the average stand age for each ESA-CCI grid cell. Only those 100 m resolution ESA-CCI grid cells, where stand age information was presented in more than 10 sub-grid pixels with 30 m resolution, were included in our

analysis. Finally, we employed a space-for-time analogy with the Chapman–Richards curve to estimate $\gamma_{rapid}^{ESA-CCI}$ for natural regrowth forests at an elevation bin of 100 m and a moving window step of 80 m (**Figure 2d**).

Similarly, to estimate the $\gamma_{rapid}^{ESA-CCI}$ for planted forests (TPFs), we first utilized a 30 m resolution global map of plantation planting years (GPY) spanning from 1982 to 2020 to identify TPF pixels. The GPY dataset includes two tree categories: tree crops and planted forests. We retained only the 100 m resolution ESA-CCI grid cells that were overlapped with more than 10 sub-grid pixels identified as "planted forest" at 30 m resolution. Subsequently, we employed a space-for-time analogy with the Chapman–Richards curve to estimate $\gamma_{rapid}^{ESA-CCI}$ for TPFs at an elevation bin of 100 m and a moving window step of 80 m (**Figure 2d**).

It is worth noting that the $\gamma_{rapid}^{ESA-CCI}$ in **Figure 1c** is the result of using both TPFs and TRFs data. For TPFs, we used the species information recorded in the GPY dataset to classify them into broadleaved and needle-leaved forests. For TRFs, we classified them into broadleaved and needle-leaved forests based on the 500 m resolution MODIS MCD12Q1 v061 land cover data[43]. Subsequently, we analyzed the elevational patterns of $\gamma_{rapid}^{ESA-CCI}$ for broadleaved and needle-leaved forests, respectively (**Figure 2e**), and between south- and north-facing slopes of mountains (**Figure 2f**).

Furthermore, we conducted an extensive analysis at the tree genus level by integrating a comprehensive *in situ* mega-database of tropical African vascular plant distributions compiled from 13 datasets[44]. In this analysis, we selectively considered tree species that met specific criteria: they had to have at least four sites in the 100m bin within a single elevation bin (100 m) and spanned at least three elevation bins between elevations of 300 to 1000 m, as there is no sufficient data for analysis above 1000 m. Moreover, we excluded data points exhibiting anomalously high biomass carbon values (> 200 $MgC \cdot ha^{-1}$) for trees aged 1 to 3 years or demonstrating an exceptionally high biomass carbon accumulation rate (> 15 $MgC \cdot ha^{-1}yr^{-1}$). Adhering to these stringent selection criteria, our analysis finally included 4 species with a total of

215 records (**Figure S4**).

Estimation of the biomass carbon accumulation rate based on a time-series 0.1° resolution live biomass dataset from 2000 to 2019 (Dataset 3)

A global vegetation live biomass dataset was generated by integrating ground inventory data and remote sensing observations, including airborne laser scanning (ALS) data and the satellite LiDAR inventory of global vegetation height structure information. This dataset was developed using a self-improving ML algorithm[37]. It provides global time-series (2000–2019) and annual live biomass data at 0.1° resolution, covering terrestrial ecosystems worldwide. Extensive validation efforts have been conducted based on over 100,000 *in situ* observations[37]. This dataset used elevation data by incorporating SRTM data into machine learning techniques to capture topographical features, thereby enhancing the accuracy of carbon stock estimates across different elevations[37]. Importantly, this dataset has found widespread application in studies pertaining to forest carbon dynamics[82-85].

In this study, the biomass carbon accumulation rate was estimated using time-series methods, as delineated in the following procedural steps.

First, we identified the TPRFs within the latitudinal range of 23.5°S-23.5°N based on MODIS MCD12C1 landcover products (version v6.1)[43] (https://lpdaac.usgs.gov/products/mcd12c1v006/), which are available from 2001 to 2019 and exhibit comparable spatial resolutions (0.05°) with the 0.1° resolution ML-derived live biomass data. Stand ages were then determined using the following approach[86-88]: (1) Firstly, tropical regions were classified into two categories: forest and non-forest lands. Forest pixels include five land cover types: evergreen needle-leaved forests, evergreen broadleaved forests, deciduous needle-leaved forests, deciduous broadleaved forests, and mixed forests; (2) Then, the commencement of growth periods was designated as the year when a transition occurred from non-forest to forest; Conversely, termination of growth periods was marked when a transition occurred from forest to non-forest; and (3) the stand age was calculated as the temporal length between

the commencement and termination of growth periods. Given the accessibility of MODIS landcover maps from 2001 to 2019, the estimated stand ages in our study encompass only immature stages, ranging from 1 year to 18 years. It is pertinent to note that, in reality, forests often commence regrowth before being visually identified in remote sensing imagery, potentially resulting in an underestimation of TPRF stand ages.

Second, to align the stand age map with the coarse spatial resolution (0.1°) of gridded forest biomass carbon data, we employed a 2×2 search window (size: 2×2 0.05° pixels) to track land cover changes. Only pixels meeting the specific criteria were included in the analysis: (1) all four pixels within the 2×2 search window were classified as non-forest lands in the year 2001; (2) more than half of the 0.05° pixels within the 2×2 search window transitioned from non-forest to forest lands during the same period; and (3) the duration of the growth period should exceed 8 years, ensuring the reliability of carbon accumulation rate calculations. Applying these criteria, a total of 1,754 0.1°×0.1°grids were selected for analysis.

Finally, for each selected 0.1° grid cell, scatter diagrams were plotted to illustrate the relationship between stand age and annual live biomass carbon. The OLS linear regression model was employed to establish a linear regression fit, with its slope designated as the biomass carbon accumulation rate (inset in **Figure 1d**). To mitigate potential uncertainties arising from data anomalies, pixels exhibiting unreasonably high carbon accumulation rates (i.e., a linear regression slope > 15 $MgC \cdot ha^{-1}yr^{-1}$) were excluded following the screening approach used in recent studies[9]. Ultimately, a total of 1, 512 TPRF grid cells were included in the final analysis (**Figure 1a**).

Exploring the elevation pattern of NEP based on model-simulated time-series carbon flux datasets spanning from 2000 to 2019 (Dataset 4)

It was observed that, on a decadal time span, nearly all augmented carbon goes into stand biomass during the initial period following afforestation, while the dynamics of soil carbon are much slower[52, 53]. NEP can therefore be used as a proxy for the biomass accumulation rate. Here, we used the time-series NEP dataset simulated by the

606 Boreal Ecosystem Productivity Simulator (BEPS) model[38], providing daily carbon
607 fluxes at a resolution of 0.072727° spanning from 1981 to 2019. We resampled the
608 time-series BEPS NEP datasets into 0.1° using the nearest-neighbor method and
609 overlapped them with the 0.1° TPRF grid cells identified for 0.1° resolution ML -
610 derived live biomass data. We then calculated the mean NEP during the growth period
611 for each TPRF grid cell derived from MODIS MCD12C1 landcover products (**Figure**
612 **1e**).

613 Furthermore, we estimated the proportion of TRFs pixels (30 m resolution)
614 identified using TMF data; and estimated the proportion of TPFs pixels (30 m
615 resolution) identified based on GPT data within each 0.1° TPRF grid cell. If the
616 proportion of TRF pixels was greater than that of TPF pixels, we classified the 0.1°
617 TPRF grid cell as a natural regrowth forest; otherwise, it was classified as a planted
618 forest. Similarly, we classified the 0.1° TPRF grid cells into broadleaved and needle-
619 leaved forests, as well as north-facing and south-facing forests, based on the land cover
620 data from MCD12C1 v061[43] and high resolution DEM data[75]. Subsequently, we
621 compared the elevational patterns of γ_{rapid} in various areas and different forest types
622 (**Figures 2g-2i**).

623

624 ***Estimation of the tree height growth rate based on GEDI tree canopy height data***

625 Tree height data were extracted from a global map of forest canopy height with 30
626 m resolution for the year 2019[39]. This map was produced by integrating LiDAR-derived
627 canopy height metrics, specifically from the GEDI level 2 product, with Landsat multi-
628 temporal surface reflectance data. This dataset underwent calibration against elevation
629 during its generation, utilizing the Shuttle Radar Topography Mission (SRTM)[75]
630 elevation data in its regression model. This calibration improves the accuracy of tree
631 height measurements, particularly in hilly or mountainous regions[39].

632 To further mitigate uncertainties in the LiDAR tree height data, a comparative
633 analysis was conducted with another widely used dataset on tree height[89]. The selection
634 process involved retaining only those pixels where the two tree height datasets

exhibited a high level of consistency, with tree height difference <±5 m (**Figure S14**).

Subsequently, we employed a space-for-time analogy to calculate the tree height growth rate (**Figure 1f)** within a specific elevation interval of 100 m using a moving window step of 80 m. This approach closely mirrors that employed for calculating the carbon accumulation rate from the ESA-CCI-derived biomass carbon data.

Exploring the impact of the differences in elevation patterns of monthly GPP and TER on the elevation patterns of NEP.

Given that the increasing elevational patterns of carbon accumulation rates were predominantly observed between March and September (**Figure 4a**), our investigation thus focused on identifying potential environmental drivers at the monthly time scale. Currently, there is a lack of available data pertaining to monthly plant carbon accumulation rates in TPRFs. Our analyses uncovered a strong correlation between the net ecosystem productivity (NEP) and the rate of plant carbon accumulation (**Figure S7a**, $P < 0.001$, slope=1.14, R^2=0.5), closely aligning with the 1:1 diagonal line. We therefore used NEP as a proxy of carbon accumulation rate to explore its potential environmental drivers in TPRFs. NEP, in this context, is defined as the difference between the amount of organic carbon fixed by photosynthesis in an ecosystem (gross primary production, GPP) and total ecosystem respiration (the sum of autotrophic and heterotrophic respiration, TER).

Worthy of note is that, although NPP is strongly linearly correlated with the carbon accumulation rate, it exhibits a much larger magnitude compared with the carbon accumulation rate (**Figure S7b**, $P < 0.001$, slope = 0.21, R^2 = 0.4). This is because biomass carbon accumulation is one of the four components of NPP, while the other three components, foliage turnover, fine root turnover, and mortality, can occupy 50% to 80% of NPP[90]. For young forests, mortality is usually very low. In tropical forests, the foliage and fine root turnovers to the soil would decompose within a few years, resulting in little change in the soil organic matter[52, 53]. Therefore, NEP performs as a better proxy for the biomass carbon accumulation rate (only stemwood and coarse root

biomass accumulates with time) compared with NPP.

For our investigation, we utilized a global carbon flux product created by Chen et al.[38] using the BEPS model. It provides the global daily GPP, TER and NEP at a spatial resolution of 0.07272727° (~10 km) from 1981 to 2019. The BEPS model is a process based diagnostic model driven by remotely sensed vegetation parameters, including biophysical variables such as Leaf Area Index (LAI), climate data (temperature and precipitation), nitrogen deposition, and atmospheric CO_2 concentrations. It initializes carbon pools based on historical net primary production (NPP) data from 1901. The model simulates carbon dynamics by stratifying biomass carbon into four pools (leaf, stem, coarse root, and fine root) and soil carbon into nine pools. Key processes include heterotrophic and autotrophic respiration, as well as net ecosystem production (NEP), which is derived from gross primary production (GPP) minus total respiration. In comparison with 15 prognostic models used by Global Carbon Project (GCP), BEPS is among the best in terms of Pearson's coefficient (R^2) and root mean square error (RMSE) between simulated and the observation-based annual global residual land sink (RLS)[38].

Although the BEPS model has a resolution of approximately 0.07272727°, it can still effectively capture differences along elevation gradients. As shown in **Figure 15**, in the Eje Volcanicao Transversal Mountain range in North America, along the latitude of 18.5°N and longitude ranging from 104°W to 96°W, there are 83 grid cells at a 10 km x 10 km resolution distributed below an elevation of 2000 m. This implies that the 10 km resolution data has sufficient capability to capture the elevation gradients below 2000 m and corresponding variations of ecological factors associated with these elevations.

Although many studies have demonstrated the satisfactory performance of the BEPS model in simulating the global carbon sink[91], some uncertainties may still remain[92]. For instance, BEPS model used MODIS LAI as an essential input data to simulate NEP, while MODIS LAI is found to be less accurate in mountainous areas compared to flatlands[93]. This may bring uncertainties in assessing the elevational

pattern of NEP[94]. Additionally, BEPS model mainly relies on the maximum carboxylation rate (V_{cmax})[95] to simulate GPP, while other photosynthesis-related parameters that may vary with elevation are mostly overlooked[96]. Although results are vertified by multiple biomass- and height- related datasets, assessments are needed in the future based on accurately simulating the GPP, TER, and NEP.

Investigation of climatic drivers influencing the elevational patterns in GPP and TER using a multiple linear regression model

Prior research has suggested that precipitation, air temperature, sunlight, vapor atmospheric dryness, and soil moisture are potential key factors in influencing the rate of carbon accumulation in tropical forests. In this study, we delved into the impacts of five key drivers, i.e. the mean air temperature (MAT), the vapor pressure deficit (VPD), precipitation (PRE), soil moisture (SM), and total photosynthetically active radiation (PAR) on the rate of carbon accumulation in restored forests (**Figures 4 and S8**). For our analyses, we used the time-series mean air temperature, VPD and precipitation from the TerraClimate global gridded meteorological and water balance variables dataset[97]. SM data was from the RSSSM global surface soil moisture dataset[98]. Total PAR data were from 0.05° resolution MODIS-derived global land products of total photosynthetically active radiation from 2000 to 2019[99]. Given the distinct spatial resolutions of these products **(Table S1)**, all variables were resampled to a 0.1° spatial resolution and monthly for the analyses. It is worth noting that air temperature, VPD, and soil moisture are represented as daily means on a monthly scale, while radiation and precipitation are presented as daily totals on a monthly scale.

Due to the significant differences in the elevation gradients of GPP and TER between months experiencing high-temperature stress and those without high-temperature stress, we then separately quantified the contributions of the elevation gradient of climatic drivers, specifically MAT, VPD (only for GPP), PRE, SM, and total PAR (only for GPP), to the elevational gradient of GPP or TER for the months under high-temperature stress and those without such stress, respectively. This quantification

was achieved by decomposing the elevation gradient of GPP ($\frac{d\mathrm{GPP}}{d\mathrm{elevation}}$) and TER ($\frac{d\mathrm{TER}}{d\mathrm{elevaion}}$) for each warm month into the additive contributions of five or four components X $\left(\frac{d\mathrm{Y}}{d\mathrm{elevation}}\right)^{\mathrm{X}}$, which was represented as the product of the partial derivative against that variable X as $\frac{\partial \mathrm{Y}}{\partial \mathrm{X}}$ and the elevation gradient of X itself as $\frac{d\mathrm{X}}{d\mathrm{elevation}}$ [80], as shown in **Equation (1)**.

$$\frac{d\mathrm{Y}}{d\mathrm{elevation}} = \frac{\partial \mathrm{Y}}{\partial \mathrm{MAT}}\frac{d\mathrm{MAT}}{d\mathrm{elevation}} + \frac{\partial \mathrm{Y}}{\partial \mathrm{VPD}}\frac{d\mathrm{VPD}}{d\mathrm{elevation}} + \frac{\partial \mathrm{Y}}{\partial \mathrm{PRE}}\frac{d\mathrm{PRE}}{d\mathrm{elevation}} + \frac{\partial \mathrm{Y}}{\partial \mathrm{SM}}\frac{d\mathrm{SM}}{d\mathrm{elevation}} + \frac{\partial \mathrm{Y}}{\partial\ \mathrm{PAR}}\frac{d\ \mathrm{PAR}}{d\mathrm{elevation}} + \varepsilon\ = \left(\frac{d\mathrm{Y}}{d\mathrm{elevation}}\right)^{\mathrm{MAT}} + \left(\frac{d\mathrm{Y}}{d\mathrm{elevation}}\right)^{\mathrm{VPD}} + \left(\frac{d\mathrm{Y}}{d\mathrm{elevation}}\right)^{\mathrm{PRE}} + \left(\frac{d\mathrm{Y}}{d\mathrm{elevation}}\right)^{\mathrm{SM}} + \left(\frac{d\mathrm{Y}}{d\mathrm{elevation}}\right)^{\mathrm{PAR}} + \varepsilon \quad (1)$$

where $\frac{\partial \mathrm{Y}}{\partial \mathrm{X}}$ represents the sensitivity of Y (GPP or TER) to an explanatory variable X (MAT, VPD, PRE, SM, total PAR [only for GPP], respectively). These sensitivities were estimated as the regression coefficients of a multiple linear regression performed with GPP or TER against all listed explanatory variables. $\frac{d\mathrm{Y}}{d\mathrm{elevation}}$ (or $\frac{d\mathrm{X}}{d\mathrm{elevation}}$) represents the sensitivity of Y or X to elevation (300-1000 m or 1000-2000 m) for each warm month. The sensitivity was calculated as the slope of the simple linear regression of mean Y (or X) values against the elevation.

Analysis of potential uncertainties arising from forest biomass carbon data, carbon accumulation rate calculations, soil fertility, types of disturbances, and various sub-regions

The reliability of forest biomass carbon data is a pivotal factor influencing the calculation precision of the biomass carbon accumulation rate. Previous studies have suggested that the ESA-CCI data may underestimate AGB in regions characterized by high AGB density (> 250 Mg ha^{-1}), particularly in low-elevation tropical forests[17]. To address this issue, we refined the bias in the ESA-CCI-derived total biomass data by integrating in situ observations, using the techniques proposed by Zhao et al.[100]. An upward trend persists in the biomass carbon accumulation rate with elevation from 300

m to 1000 m based on the adjusted biomass carbon data (slope = 0.20±0.05 MgC·ha^{-1} yr^{-1} m^{-1}; mean carbon accumulation rate = 2.94±0.28 MgC·ha^{-1} yr^{-1}, **Figure S16**). This consistency aligns with our findings based on the original ESA-CCI-derived total biomass carbon data (slope = 0.23±0.04 MgC·ha^{-1}yr^{-1}m^{-1}; the mean rate = 2.85±0.28 MgC·ha^{-1}yr^{-1}, **Figure 1e**).

To determine the biomass carbon accumulation rate of TPRFs during the rapid growth phase across various elevations, this study initially focused on data points where the biomass carbon was below 80% of that in old-growth forests for analysis. Subsequently, we adjusted these thresholds to 70% and 90% to examine their potential effects on the elevation dependence of the biomass carbon accumulation rate (**Figure 3f**). Results reveal very slight variations in the slopes of the linear regression curve between biomass carbon accumulation rate and elevation (for altitudes between 300 m and 1000 m: 70% threshold: slope = 0.11±0.05 MgC·ha^{-1}yr^{-1}m^{-1}; 80% threshold: slope = 0.23±0.04 MgC·ha^{-1}yr^{-1}m^{-1}; 90% threshold: slope = 0.19±0.06 MgC·ha^{-1}yr^{-1}m^{-1}). We further verified the results of this method for detecting the rapid growth stand age (age_{rapid}) with the observed age_{rapid}, which was determined as the stand age when there was a break point change in the relationship of five-years carbon accumulation rate and age. This time point was identified using segmented regression models[101] (**Figure S3**). Results indicated that the estimated age_{rapid} using the 80% peak biomass coincided well with those estimated from the derivative change of accumulation rates (**Figure 3e**).

Human activities have the potential to influence the biomass carbon accumulation rate in TPRFs[18]. Here, we both tested the intrinsic influences from previous land use types before converting to TPRFs and external influences from surrounding non-forest lands. The fraction of non-forest lands (urban and croplands) nearby the TPRFs (neighboring 10×10 1km resolution pixels) decreases with elevation, contributing slightly to the increasing elevational trend of the carbon accumulation rate in TPRFs (**Figure S10**). In contrast, the elevational patterns in TPRFs that used to be shifting cultivation and pasture both show marginally small variations (**Figure S13**). Worthy of

note is that, we did not analyze other land use types, such as fire, clear-cut harvest, and mining, due to a lack of sufficient biomass carbon data across the studied elevation range.

Moreover, organic carbon (https://openlandmap.org), total phosphorus[102], sand and clay concentrations (https://openlandmap.org) in soil all exhibited insignificant trends (P>0.05) along with elevation (**Figure S17**), indicating a limited influence of soil fertility on the elevation dependence of carbon accumulation rate.

All these additional analyses confirm the robustness of our findings regarding the elevational patterns of biomass carbon accumulation rates in TPRFs.

Resource availability

Lead contact

For further information on the analysis, please contact the corresponding author, Yongxian Su (yxsu@rcees.ac.cn).

Materials availability

This study has not generated any new, unique materials.

Data and Code Availability

All the original datasets used in this research are publicly available from their sources：a global Forest Carbon database (ForC): https://github.com/forc-db; ESA-CCI AGB map: https://catalogue.ceda.ac.uk/uuid/af60720c1e404a9e9d2c145d2b2ead4e; 0.1° global live biomass carbon: https://zenodo.org/records/4161694; Carbon flux (GPP/TER/NPP/NEP) simulations obtained from the BEPS model: https://datadryad.org/stash/landing/show?id=doi%3A10.5061%2Fdryad.q573n5tgb; Jung et al.'s FLUXCOM data: https://fluxnet.org/data/fluxnet2015-dataset/ ; Tree height dataset: https://glad.umd.edu/dataset/GLCLUC2020; https://www.nature.com/articles/s41559-023-02206-6; JRC-TMF dataset (https://forobs.jrc.ec.europa.eu/TMF/ download/); MCD12C1 v061 land cover: https://lpdaac.usgs.gov/products/mcd12c1v061/; TerraClimate MAT, VPD, PRE: https://www.climatologylab.org/terraclimate.html; Global remote-sensing-based

surface soil moisture (RSSSM): https://doi.pangaea.de/10.1594/PANGAEA.912597; BESS total PAR: https://www.environment.snu.ac.kr/bess-rad; Plantation year dataset: https://figshare.com/articles/dataset/A_global_map_of_planting_years_of_plantations/19070084/1; Global reforestation potential map: https://zenodo.org/records/883444; Global soil total phosphorus concentration dataset: https://doi.org/10.6084/m9.figshare.14583375.v9; Global soil organic/sandy/clay carbon dataset: https://zenodo.org/records/2525663; https://doi.org/10.5281/zenodo.2525662; https://doi.org/10.5281/zenodo.2525553; Tree species dataset: https://gdauby.github.io/rainbio/index.html

The code used for this analysis is available in a Zenodo repository at https://doi.org/10.5281/zenodo.13922571 (ref.103).

CONTRIBUTIONS

Y.S. and X.C. designed the study and wrote the initial manuscript. Y.S., C.Z., W. Y. and X.L. collected the data and performed the analysis. P.C., S.C.P, O.L.P., J.S., A.C., J.M.C., J.L., J.C., C.E.D., F.T., Y.Q.L., Y.L., Z.Y., D.H., S.T. and Y.Z. contributed to discuss the scientific question and revise the manuscript. All authors reviewed, revised and approved the manuscript.

COMPETING INTEREST STATEMENT

We thank Dr. Ranga Myneni for his valuable suggestions to improve the manuscript. The authors declare no competing interests.

ACKONWLEDGEMENTS

This study was supported by the National Natural Science Foundation of China (grant nos. 42471326, 41971275, 31971458, 42001299 and U21A6001).

833 **TABLE**

834 **Table 1** Independent biomass, carbon, and height datasets and corresponding methods to quantify the γ_{rapid} (see **Experimental Procedure** for
835 details).

NO.	Biomass carbon proxies	Biomass carbon data sources	Stand age data sources	Stand age estimation method	γ_{rapid} estimation method	Acronyms
Dataset 1	forest biomass (*in situ*, global)	Smithsonian Institution's Global Forest Carbon (ForC) database [36] and other in-situ datasets[9]		Original stand age records	γ_{rapid} was determined as the slope of linear regression fit between observed forest biomass carbon densities and the stand age of TPRFs where biomass carbon was less than 80% of old-growth forests (stand age $\geqslant$ 100 years) simulated in the Chapman–Richards curve using the space-for-time method.	γ_{rapid}^{GFC}
Dataset 2	Aboveground forest biomass (100m, global, 2018)	ESA-CCI[17]	Cover change map of tropical moisture forest (TMF) (30m, Tropical, 1982-2019)[41] and global plantation years dataset (GPY) (30m, global, 1982-2020)[42]	Stand age of natural regrowth forests was determined based on TMF cover change data. Stand age of planted forests was calculated based on GPY dataset.		$\gamma_{rapid}^{ESA-CCI}$
Dataset 5	Forest canopy height dataset (30m, global, 2019)	GEDI LiDAR dataset[39]				γ_{rapid}^{GEDI}
Dataset 3	Total live woody biomass (0.1°, global, 2000-2019)	Machine-learning (ML)-derived terrestrial live biomass dataset[37]	MODIS MCD12C1 landcover products (0.05°, global, 2001-2019)[43]	Stand age was calculated based on the time series MODIS MCD12C1 land cover dataset.	γ_{rapid} was determined as the slope of linear regression fit between biomass carbon and stand age of TPRFs using the time-series analysis method.	γ_{rapid}^{ML}
Dataset 4	Net ecosystem productivity (0.07273°, global, 1981-2019)	BEPS model[38]				γ_{rapid}^{BEPS}

836

FIGURE CAPTIONS

Figure 1. Average carbon accumulation rates (γ_{rapid}) in TPRFs by elevation up to 2000 m above mean sea level (a.m.s.l.). a, *In-situ* sites of field measurements and grid cells of raster-based data used in this study. Purple triangles represent *in situ* sites of forest biomass data used for γ_{rapid}^{GFC} estimation. The dots in different green colors represent the 100 m × 100 m grid cells used for $\gamma_{rapid}^{ESA-CCI}$ or γ_{rapid}^{GEDI} estimation. Black dots represent the 0.1° × 0.1° grid cells used for γ_{rapid}^{ML} or γ_{rapid}^{BEPS} estimation. **b-f,** Elevation pattern of annual γ_{rapid}^{GFC} (**b**), $\gamma_{rapid}^{ESA-CCI}$ (**c**), γ_{rapid}^{ML} (**d**), γ_{rapid}^{BEPS} (**e**) and γ_{rapid}^{GEDI} (**f**), respectively. The dashed lines represent the linear fit between γ_{rapid} and elevation, with shading representing the 95% confidence interval. Significant relationships ($P \leqslant 0.05$) are denoted in blue, and insignificant ones ($P > 0.05$) in grey. In panels **b**, **c**, and **f**, each histogram represents the slope of the corresponding ordinary least squares (OLS) regression line (orange dashed lines in the inset plot)[9] between biomass carbon and age during the rapid growth stage of forest (γ_{rapid}) before reaching maturity (black dashed vertical lines in the inset plot, representing 80% of its maximum biomass carbon and grey dashed lines in the inset plots represent the fitted Chapman–Richards curve) within each elevation bin (100±50 m in an 80 m step) using the space-for-time analogy. Color gradients of histogram graphs indicate the R^2 between simulated and observed γ_{rapid} in each elevation bin. Error bars indicate one standard error. In panel **d**, black dots represent the slope of the corresponding linear regression curve (orange dashed lines in inset plot) between model-simulated plant carbon densities and stand age, using the time-series data from each TPRF. In panel **e**, each black triangle represents the mean NEP of each targeted TPRF, with error bars indicating one standard error. Numbers at the top of panels **d** and **e** represent the slope of linear regression between γ_{rapid} and elevation, with significance indicated in the legend as • $P<0.5$, * $P<0.1$, ** $P<0.01$, and *** $P<0.001$. Notably, the assessment of the relationship between γ_{rapid} and elevation is only up to 1300 m based on in-situ data

(panel **a**), while analyses using other datasets (panels **b-f**) are up to 2000 m.

Figure 2. Elevational patterns of average carbon accumulation rates (γ_{rapid}) derived from three datasets across various forest characteristics at elevations up to 2000 m above mean sea level (a.m.s.l.). a, d, g, The elevational patterns of γ_{rapid}^{GFC} (**a**), $\gamma_{rapid}^{ESA-CCI}$ (**d**) and γ_{rapid}^{BEPS} (**g**) in natural regrowth compared to planted forests. The same as for **a, d, g**, but in broadleaved compared to needle-leaved forests. **c, f, i,** The same as for **a, d, g**, but in north-facing compared to south-facing slopes of mountains. In panels **a-f**, each dot represents the mean γ_{rapid} for each elevation bin (100±50 m in an 80 m step), estimated based on the Chapman–Richards curve, with the error bars indicating one standard error in each elevational bin. In **g-i**, each dot represents the mean NEP for each targeted forest grid cell, with the error bars indicating one standard error. The lines in panels **a-i** represent the linear fit between γ_{rapid} and elevation, with shading indicating the 95% confidence interval. Significant relationships ($P \leqslant 0.05$) are denoted by solid lines, and insignificant ones ($P > 0.05$) are represented by dashed lines. Numbers at the top of panels represent the slope of linear regression between γ_{rapid} and elevation, with significance indicated in the legend as • $P<0.5$, * $P<0.1$, ** $P<0.01$, and *** $P<0.001$.

Figure 3. The influence of stand age on the elevational pattern of γ_{rapid}. a, Illustrations of the fixed stand age approach for calculating the carbon accumulation rate. The slopes of three blue dashed curves represent the carbon accumulation rates during T_1 -T_2, T_2 -T_3 and T_1 -T_3 time periods, respectively. **b**, Illustrations of the carbon accumulation window approach for calculating γ_{rapid}. The slopes of red solid and red dashed curves represent the γ_{rapid} at low- (i.e., < 500 m) and mid-elevations (i.e., 500 -1500 m[48, 49]), respectively. The selected window is intensified when carbon accumulation reaches 80% of the median biomass carbon of old-growth forests (stand age > 100 years). The black solid and dashed curves represent the Chapman–Richards curves for TPRFs at low- and mid-elevations, respectively. **c**, Sensitivity of total biomass carbon derived from ESA-CCI data to elevation (i.e., 300-1000 m and 1000-

2000 m) across different stand ages. Sensitivity is defined as the slope of the linear regression curve illustrating the relationship between biomass carbon and elevation within each one-year stand age bin (**Figure S6**). **d,** Elevational patterns of biomass carbon accumulate rates using diverse stand age windows (i.e., 20, 24, 28, and 32 years of age) to locate the analysis period along the Chapman–Richards curve, as used in previous studies[9]. **e**, Comparisons between the stand ages (age_{rapid}) with rapid accumulation rate identified using 80% peak biomass thresholds and observed age_{rapid}, which was determined as the stand age when there was an abrupt change with the relationship with stand age as stand age increases. **f,** Elevational patterns of biomass carbon accumulate rates using different peak biomass thresholds (i.e., from zero to the time of reaching 70%, 80% and 90% of the maximum value). In panels **d and f**, each dot represents the slope of the corresponding ordinary least squares (OLS) regression curve between ESA-CCI-derived total biomass carbon and the stand age within given age windows (**d**) or using different peak biomass thresholds (**f**) at a given elevation bin (100±50 m in an 80 m step). The colored curves depict the linear regressions between γ_{rapid} and elevation, ranging from 300 m to 1000 m and 1000 m to 2000 m, respectively.

Figure 4. Impact of climatic factors on the elevation patterns of seasonal carbon fluxes. a-b, Linear regressions between each month's GPP (red), TER (blue), NEP (orange) simulated by the BEPS model (**Dataset 4**)[38] and elevation for ranges of 300-1000 m (**a**) and 1000-2000 m (**b**), respectively. **c-f,** Linear regressions between each month's mean air temperature (MAT) (**c-d**) or precipitation (PRE) (**e-f**) and elevation for ranges of 300-1000 m (**c, e**) and 1000-2000 m (**d, f**), respectively. Shadings indicate 95% confidence intervals. Significant relationships ($P \leqslant 0.05$) are shown in solid lines, and non-significant relationships ($P > 0.05$) in dashed lines. **g-h**, Changes in monthly GPP and TER with MAT (**g**) or PRE (**h**), respectively. Each dot denotes the median value of GPP (red) (or TER [blue]) within a 1°C MAT bin (or 20mm PRE bin), respectively. Error bars depict one standard deviation. The dashed curves are fitted using local polynomial regression based on the 'loess' function in the R 'stats' package

with default settings. The solid curves in panel **g** represent the linear fitting regressions between the GPP, TER, and MAT for MAT higher than 24°C, while in panel **h** represent the linear fitting regressions between the GPP, TER, and PRE for PRE lower than 150 mm. In panels **c-d** and **g,** the brown background indicates that MAT is ⩾24°C. In panel **h,** the light blue background indicates that PRE <150 mm. **i-j,** Absolute contributions of the elevational trends in climate factors to the elevational variations in GPP and TER determined by the multiple linear regression model for months with MAT ⩾ 24°C (**i**) and < 24°C (**j**), respectively. Error bars represent one standard error. The asterisks indicate the *P* values: * P<0.05, ** P<0.01, and *** P<0.001.

Figure 5. Elevational patterns of γ_{rapid}^{BEPS} and the underlying mechanisms across four mountains. a, Locations of four tropical mountains: the Serra do Espinhaço mountain in South America (SMS), the Ethiopian Highlands mountain in Africa (EH), the Serra do Espinhaço mountain in South America (SE), and the Eastern Ghats mountain in Asia (EG)**. b-e,** Elevational pattern of γ_{rapid}^{BEPS} in four mountains. Blue dashed curves and red solid lines represent the smoothed trend fitted by a generalized additive model (GAM) and the linear fit at both sides of each threshold, respectively. **f,** Elevational pattern of mean air temperature and precipitation in four mountains. **g,** The optimal elevation, i.e., the places with the highest values of γ_{rapid}^{BEPS} in four mountains. **h,** Elevational sensitivity of γ_{rapid}^{BEPS} below (green histogram) and above (grey histogram) the optimal elevation in four mountains. **i-l,** Absolute contributions of the elevational trends in climate factors to the elevational variations in GPP and TER determined by the multiple linear regression model for months with MAT ⩾ 24°C in SMS (**i**), EH (**j**), SE (**k**), and EG (**l**), respectively. **m-p,** Absolute contributions of the elevational trends in climate factors to the elevational variations in GPP and TER for months with MAT < 24°C in corresponding four mountains. Error bars represent one standard error.

References:

1. Pan, Y., Birdsey, R. A., Fang, J., Houghton, R., Kauppi, P. E., Kurz, W. A., Phillips, O. L., Shvidenko, A., Lewis, S. L., Canadell, J. G., Ciais, P., Jackson, R. B., Pacala, S. W., McGuire, A. D., Piao, S., Rautiainen, A., Sitch, S., & Hayes, D. 2011. A large and persistent carbon sink in the world's forests. Science, 333(6045): 988-993.
2. Harris, N. L., Gibbs, D. A., Baccini, A., Birdsey, R. A., de Bruin, S., Farina, M., Fatoyinbo, L., Hansen, M. C., Herold, M., Houghton, R. A., Potapov, P. V., Suarez, D. R., Roman-Cuesta, R. M., Saatchi, S. S., Slay, C. M., Turubanova, S. A., & Tyukavina, A. 2021. Global maps of twenty-first century forest carbon fluxes. Nature Climate Change, 11(3): 234-240.
3. Gatti, L. V., Basso, L. S., Miller, J. B., Gloor, M., Gatti Domingues, L., Cassol, H. L. G., Tejada, G., Aragão, L. E. O. C., Nobre, C., Peters, W., Marani, L., Arai, E., Sanches, A. H., Corrêa, S. M., Anderson, L., Von Randow, C., Correia, C. S. C., Crispim, S. P., & Neves, R. A. L. 2021. Amazonia as a carbon source linked to deforestation and climate change. Nature, 595(7867): 388-393.
4. Mo, L., Zohner, C. M., Reich, P. B., Liang, J., de Miguel, S., Nabuurs, G.-J., Renner, S. S., van den Hoogen, J., Araza, A., Herold, M., Mirzagholi, L., Ma, H., Averill, C., Phillips, O. L., Gamarra, J. G. P., Hordijk, I., Routh, D., Abegg, M., Adou Yao, Y. C., Alberti, G., Almeyda Zambrano, A. M., Alvarado, B. V., Alvarez-Dávila, E., Alvarez-Loayza, P., Alves, L. F., Amaral, I., Ammer, C., Antón-Fernández, C., Araujo-Murakami, A., Arroyo, L., Avitabile, V., Aymard, G. A., Baker, T. R., BaĹ , azy, R., Banki, O., Barroso, J. G., Bastian, M. L., Bastin, J.-F., Birigazzi, L., Birnbaum, P., Bitariho, R., Boeckx, P., Bongers, F., Bouriaud, O., Brancalion, P. H. S., Brandl, S., Brearley, F. Q., Brienen, R., Broadbent, E. N., Bruelheide, H., Bussotti, F., Cazzolla Gatti, R., César, R. G., Cesljar, G., Chazdon, R. L., Chen, H. Y. H., Chisholm, C., Cho, H., Cienciala, E., Clark, C., Clark, D., Colletta, G. D., Coomes, D. A., Cornejo Valverde, F., Corral-Rivas, J. J., Crim, P. M., Cumming, J. R., Dayanandan, S., de Gasper, A. L., Decuyper, M., Derroire, G. r., DeVries, B., Djordjevic, I., Dolezal, J., Dourdain, A. l., Engone Obiang, N. L., Enquist, B. J.,

978 Eyre, T. J., Fandohan, A. B., Fayle, T. M., Feldpausch, T. R., Ferreira, L. V., Finér,
979 L., Fischer, M., Fletcher, C., Frizzera, L., Gianelle, D., Glick, H. B., Harris, D. J.,
980 Hector, A., Hemp, A., Hengeveld, G., Hérault, B., Herbohn, J. L., Hillers, A.,
981 Honorio Coronado, E. d. N., Hui, C., Ibanez, T., Imai, N., JagodziĹ„ski, A. M.,
982 Jaroszewicz, B., Johannsen, V. K., Joly, C. A., Jucker, T., Jung, I., Karminov, V.,
983 Kartawinata, K., Kearsley, E., Kenfack, D., Kennard, D. K., Kepfer-Rojas, S.,
984 Keppel, G., Khan, M. L., Killeen, T. J., Kim, H. S., Kitayama, K., Köhl, M., Korjus,
985 H., Kraxner, F., Kucher, D., Laarmann, D., Lang, M., Lu, H., Lukina, N. V., Maitner,
986 B. S., Malhi, Y., Marcon, E., Marimon, B. S., Marimon-Junior, B. H., Marshall, A.
987 R., Martin, E. H., Meave, J. A., Melo-Cruz, O., Mendoza, C., Mendoza-Polo, I.,
988 Miscicki, S., Merow, C., Monteagudo Mendoza, A., Moreno, V. S., Mukul, S. A.,
989 Mundhenk, P., Nava-Miranda, M. a. G., Neill, D., Neldner, V. J., Nevenic, R. V.,
990 Ngugi, M. R., Niklaus, P. A., Oleksyn, J., Ontikov, P., Ortiz-Malavasi, E., Pan, Y.,
991 Paquette, A., Parada-Gutierrez, A., Parfenova, E. I., Park, M., Parren, M.,
992 Parthasarathy, N., Peri, P. L., Pfautsch, S., Picard, N., Piedade, M. T. F., Piotto, D.,
993 Pitman, N. C. A., Poulsen, A. D., Poulsen, J. R., Pretzsch, H., Ramirez Arevalo, F.,
994 Restrepo-Correa, Z., Rodeghiero, M., Rolim, S. G., Roopsind, A., Rovero, F.,
995 Rutishauser, E., Saikia, P., Salas-Eljatib, C., Saner, P., Schall, P., Schelhaas, M.-J.,
996 Schepaschenko, D., Scherer-Lorenzen, M., Schmid, B., Schöngart, J., Searle, E. B.,
997 Seben, V. r., Serra-Diaz, J. M., Sheil, D., Shvidenko, A. Z., Silva-Espejo, J. E.,
998 Silveira, M., Singh, J., Sist, P., Slik, F., Sonké, B., Souza, A. F., StereĹ„czak, K. J.,
999 Svenning, J.-C., Svoboda, M., Swanepoel, B., Targhetta, N., Tchebakova, N., ter
1000 Steege, H., Thomas, R., Tikhonova, E., Umunay, P. M., Usoltsev, V. A., Valencia,
1001 R., Valladares, F., van der Plas, F., Van Do, T., van Nuland, M. E., Vasquez, R. M.,
1002 Verbeeck, H., Viana, H., Vibrans, A. C., Vieira, S., von Gadow, K., Wang, H.-F.,
1003 Watson, J. V., Werner, G. D. A., Wiser, S. K., Wittmann, F., Woell, H., Wortel, V.,
1004 Zagt, R., Zawiła-Niedźwiecki, T., Zhang, C., Zhao, X., Zhou, M., Zhu, Z.-X., Zo-Bi,
1005 I. C., Gann, G. D., & Crowther, T. W. 2023. Integrated global assessment of the
1006 natural forest carbon potential. Nature, 1-10.

5. Watson, R., Noble, I., Bolin, B., Ravindranath, N. H., Verardo, D. J., & Dokken, D. 2000. Land use, land-use change, and forestry. A special report of the Intergovernmental Panel on Climate Change. Cambridge University Press, UK
6. Turner, E. C., & Foster, W. A. 2009. The impact of forest conversion to oil palm on arthropod abundance and biomass in Sabah, Malaysia. Journal of Tropical Ecology, 2009, 25(1): 23-30.
7. Houghton, R. A. 2012. Carbon emissions and the drivers of deforestation and forest degradation in the tropics. Current Opinion in Environmental Sustainability, 4(6), 597-603.
8. Roe, S., Streck, C., Beach, R., Busch, J., Chapman, M., Daioglou, V., Deppermann, A., Doelman, J., Emmet-Booth, J., Engelmann, J., Fricko, O., Frischmann, C., Funk, J., Grassi, G., Griscom, B., Havlik, P., Hanssen, S., Humpenöder, F., Landholm, D., Lomax, G., Lehmann, J., Mesnildrey, L., Nabuurs, GJ., Popp, A., Rivard, C., Sanderman, J., Sohngen, B., Smith, P., Stehfest, E., Woolf, D., & Lawrence, D. 2021. Land-based measures to mitigate climate change: Potential and feasibility by country. Global Change Biology, 27, 6025-6058.
9. Cook-Patton, S. C., Leavitt, S. M., Gibbs, D., Harris, N. L., Lister, K., Anderson-Teixeira, K. J., Briggs, R. D., Chazdon, R. L., Crowther, T. W., Ellis, P. W., Griscom, H. P., Herrmann, V., Holl, K. D., Houghton, R. A., Larrosa, C., Lomax, G., Lucas, R., Madsen, P., Malhi, Y., Paquette, A., Parker, J. D., Paul, K., Routh, D., Roxburgh, S., Saatchi, S., van den Hoogen, J., Walker, W. S., Wheeler, C. E., Wood, S. A., Xu, L., & Griscom, B. W. 2020. Mapping carbon accumulation potential from global natural forest regrowth. Nature, 585(7826): 545-550.
10. Heinrich, V. H. A., Dalagnol, R., Cassol, H. L. G., Rosan, T. M., de Almeida, C. T., Silva Junior, C. H. L., Campanharo, W. A., House, J. I., Sitch, S., Hales, T. C., Adami, M., Anderson, L. O., & Aragão, L. E. O. C. 2021. Large carbon sink potential of secondary forests in the brazilian amazon to mitigate climate change. Nature Communications, 12(1): 1785.
11. Fahey, T. J., Sherman, R. E., & Tanner, E. V. 2016. Tropical montane cloud forest:

Environmental drivers of vegetation structure and ecosystem function. Journal of Tropical Ecology, 32(5): 355-367.

12. Malhi et al. 2016. The variation of productivity and its allocation along a tropical elevation gradient: a whole carbon budget perspective https://nph.onlinelibrary.wiley.com/doi/10.1111/nph.14189
13. Bernal et al. 2018 Global carbon dioxide removal rates from forest landscape restoration activities https://cbmjournal.biomedcentral.com/articles/10.1186/s13021-018-0110-8
14. Bukoski, J.J., Cook-Patton, S.C., Melikov, C., Ban, H., Chen, J. L., Goldman, E. D., Harris, N. L., & Potts, M. D. 2022. Rates and drivers of aboveground carbon accumulation in global monoculture plantation forests. Nature Communications, 13, 4206.
15. Elias, F., Ferreira, J., Resende, A.F., Berenguer, E., França, F., Smith, C. C., Schwartz, G., Nascimento, R. O., Guedes, M., Rossi, L. C., Seixas, M. M. M., Silva, C. M., & Barlow, J. 2022. Comparing contemporary and lifetime rates of carbon accumulation from secondary forests in the eastern Amazon. Forest Ecology and Management, 508, 120053.
16. Yu, K., Chen, H. Y. H., Gessler, A., Pugh, T. A. M., Searle, E. B., Allen, R. B., Pretzsch, H., Ciais, P., Phillips, O. L., Brienen, R. J. W., Chu, C., Xie, S., Ballantyne, A. P. 2024. Forest demography and biomass accumulation rates are associated with transient mean tree size vs. density scaling relations. PNAS Nexus, 2024 Feb 17;3(2):pgae008.
17. Santoro, M., Cartus, O. 2021. ESA Biomass Climate Change Initiative (Biomass_cci): Global datasets of forest above-ground biomass for the years 2010, 2017 and 2018, v2. Centre for Environmental Data Analysis. http://dx.doi.org/10.5285/84403d09cef3485883158f4df2989b0c.
18. Heinrich, V. H. A., Vancutsem, C., Dalagnol, R., Rosan, T. M., Fawcett, D., Silva-Junior, C. H. L., Cassol, H. L. G., Achard, F. d. r., Jucker, T., Silva, C. A., House, J., Sitch, S., Hales, T. C., & Aragão, L. E. O. C. 2023. The carbon sink of secondary

and degraded humid tropical forests. Nature, 615(7952): 436-442.

19. Aplet, G. H., & Vitousek, P. M. 1994. An age--altitude matrix analysis of hawaiian rain-forest succession. Journal of Ecology: 137-147.
20. Dossa, G. G., Paudel, E., Fujinuma, J., Yu, H., Chutipong, W., Zhang, Y., Paz, S., & Harrison, R. D. 2013. Factors determining forest diversity and biomass on a tropical volcano, mt. Rinjani, lombok, indonesia. PLoS One, 8(7): e67720.
21. Raich, J. W., Russell, A. E., Kitayama, K., Parton, W. J., & Vitousek, P. M. 2006. Temperature influences carbon accumulation in moist tropical forests. Ecology, 87(1): 76-87.
22. Moser, G. 2008. Elevation effects on key processes of carbon cycling in south ecuadorian mountain forests. Citeseer.
23. Alves, L. F., Vieira, S. A., Scaranello, M. A., Camargo, P. B., Santos, F. A., Joly, C. A., & Martinelli, L. A. 2010. Forest structure and live aboveground biomass variation along an elevational gradient of tropical atlantic moist forest (Brazil). Forest ecology and management, 260(5): 679-691.
24. Rosenfield, M. F., & Souza, A. F. 2014. Forest biomass variation in southernmost Brazil: The impact of araucaria trees. Revista de Biología Tropical, 62(1): 335-348.
25. Girardin, C. A. J., Malhi, Y., Aragão, L. E. O. C., Mamani, M., Huaraca Huasco, W., Durand, L., Feeley, K. J., Rapp, J., Silva-Espejo, J. E., Silman, M., Salinas, N., & Whittaker, R. J. 2010. Net primary productivity allocation and cycling of carbon along a tropical forest elevational transect in the peruvian andes. Global Change Biology, 16(12): 3176-3192.
26. Marshall, A. R., Willcock, S., Platts, P. J., Lovett, J. C., Balmford, A., Burgess, N. D., Latham, J. E., Munishi, P. K., Salter, R., & Shirima, D. 2012. Measuring and modelling above-ground carbon and tree allometry along a tropical elevation gradient. Biological Conservation, 154: 20-33.
27. Ensslin, A., Rutten, G., Pommer, U., Zimmermann, R., Hemp, A., & Fischer, M. 2015. Effects of elevation and land use on the biomass of trees, shrubs and herbs at Mount Kilimanjaro. Ecosphere, 6(3): 1-15.

28. Alrutz, M., Gómez-Díaz J A., Schneidewind, U., Krömer, T., & Kreft, H. 2022. Forest structural parameters and aboveground biomass in old-growth and secondary forests along an elevational gradient in Mexico. Botanical Sciences, 100(1): 67-85.
29. Feng, Y., Ziegler, A. D., Elsen, P. R., Liu, Y., He, X., Spracklen, D. V., Holden, J., Jiang, X., Zheng, C., & Zeng, Z. 2021. Upward expansion and acceleration of forest clearance in the mountains of southeast asia. Nature Sustainability, 4(10): 892-899.
30. Spracklen, D., & Righelato, R. 2014. Tropical montane forests are a larger than expected global carbon store. Biogeosciences, 11(10): 2741-2754.
31. Poorter, L., Bongers, F., Aide, T. M., Almeyda, Zambrano, A. M., Balvanera, P., Becknell, J. M., Boukili, V., Brancalion, P. H., Broadbent, E. N., Chazdon, R. L., Craven, D., de Almeida-Cortez JS, Cabral, G. A., de Jong, B. H., Denslow, J. S., Dent, D. H., DeWalt, S. J., Dupuy, J. M., Durán, S. M., Espírito-Santo, M. M., Fandino, M. C., César, R. G., Hall, J. S., Hernandez-Stefanoni, J. L., Jakovac, C. C., Junqueira, A. B., Kennard, D., Letcher, S. G., Licona, J. C., Lohbeck, M., Marín-Spiotta, E., Martínez-Ramos, M., Massoca, P., Meave, J. A., Mesquita, R., Mora, F., Muñoz, R., Muscarella, R., Nunes, Y. R,, Ochoa-Gaona, S., de Oliveira, A. A., Orihuela-Belmonte, E., Peña-Claros, M., Pérez-García, E. A., Piotto, D., Powers, J. S., Rodríguez-Velázquez, J., Romero-Pérez, I. E., Ruíz, J., Saldarriaga, J. G., Sanchez-Azofeifa, A., Schwartz, N. B., Steininger, M. K., Swenson, N. G., Toledo, M., Uriarte, M., van Breugel, M., van der Wal, H., Veloso, M. D., Vester, H. F., Vicentini, A., Vieira, I. C., Bentos, T. V., Williamson, G. B., Rozendaal, D. M. 2016. Biomass resilience of Neotropical secondary forests. Nature, 2016, 530(7589): 211-214.
32. Requena, S. D., Rozendaal, D. M. A., De Sy. V., Phillips, O. L., Alvarez-Dávila, E., Anderson-Teixeira, K., Araujo-Murakami, A., Arroyo, L., Baker, T. R., Bongers, F., Brienen, R. J. W., Carter, S., Cook-Patton, S. C., Feldpausch, T. R., Griscom, B. W., Harris, N., Hérault, B., Honorio, Coronado, E. N., Leavitt, S. M., Lewis, S. L., Marimon, B. S., Monteagudo Mendoza, A., Kassi N'dja, J., N'Guessan, A. E.,

Poorter, L., Qie, L., Rutishauser, E., Sist, P., Sonké, B., Sullivan, M. J. P., Vilanova, E., Wang, M. M. H., Martius, C., & Herold, M. 2019. Estimating aboveground net biomass change for tropical and subtropical forests: Refinement of IPCC default rates using forest plot data. Global Change Biology, 2019, 25(11): 3609-3624.

33. Holl, K. D., & Brancalion, P. H. 2020. Tree planting is not a simple solution. Science, 368(6491): 580-581.
34. Verburg, R., Slik, F., Heil, G., Roos, M., Baas, P., Hillegers, P., Longh, H. D. 2021. Secondary forest succession of rainforests in East Kalimantan: a preliminary data analysis. The balance between biodiversity conservation and sustainable use of tropical rain forest, 2001: 151-160.
35. Richards, F. J. A flexible growth function for empirical use. J. Exp. Bot. 10, 290–301 (1959).
36. Anderson-Teixeira, K. J., Wang, M. M., McGarvey, J. C., Herrmann, V., Tepley, A. J., Bond-Lamberty, B., & LeBauer, D. S. 2018. ForC: A global database of forest carbon stocks and fluxes. Ecology, 99(6): 1507.
37. Xu, L., Saatchi, S. S., Yang, Y., Yu, Y., Pongratz, J., Bloom, A. A., Bowman, K., Worden, J., Liu, J., Yin, Y., Domke, G., McRoberts, R. E., Woodall, C., Nabuurs, G.-J., de-Miguel, S., Keller, M., Harris, N., Maxwell, S., & Schimel, D. Changes in global terrestrial live biomass over the 21st century. Science Advances, 7(27): eabe9829.
38. Chen, J. M., Ju, W., Ciais, P., Viovy, N., Liu, R., Liu, Y., & Lu, X. 2019. Vegetation structural change since 1981 significantly enhanced the terrestrial carbon sink. Nature Communications, 10(1): 4259.
39. Potapov, P., Li, X., Hernandez-Serna, A., Tyukavina, A., Hansen, M. C., Kommareddy, A., Pickens, A., Turubanova, S., Tang, H., Silva, C. E., Armston, J., Dubayah, R., Blair, J. B., & Hofton, M. 2021. Mapping global forest canopy height through integration of GEDI and landsat data. Remote Sensing of Environment, 253: 112165.
40. Zeng, Z., Wang, D., Yang, L., Wu, J., Ziegler, A. D., Liu, M., Ciais, P., Searchinger,

T. D., Yang, Z.-L., Chen, D., Chen, A., Li, L. Z. X., Piao, S., Taylor, D., Cai, X., Pan, M., Peng, L., Lin, P., Gower, D., Feng, Y., Zheng, C., Guan, K., Lian, X., Wang, T., Wang, L., Jeong, S.-J., Wei, Z., Sheffield, J., Caylor, K., & Wood, E. F. 2021. Deforestation-induced warming over tropical mountain regions regulated by elevation. Nature Geoscience, 14(1): 23-29.

41. Vancutsem, C., Achard, F., Pekel, J. F., Vieilledent, G., Carboni, S., Simonetti, D., Gallego, J., Aragao, L. E. O. C., & Nasi, R. 2021. Long-term (1990-2019) monitoring of forest cover changes in the humid tropics. Science Advances, 7(10): eabe1603.
42. Du, Z., Yu, L., Yang, J., Xu, Y., Chen, B., Peng, S., Zhang, T., Fu, H., Harris, N. & Gong, P. 2022. A global map of planting years of plantations. Scientific Data, 9, 1-9.
43. Friedl, M., Sulla-Menashe, D. 2022. MODIS/Terra+Aqua Land Cover Type Yearly L3 Global 500m SIN Grid V061 [Data set]. NASA EOSDIS Land Processes Distributed Active Archive Center. Accessed 2024-08-21 from https://doi.org/10.5067/MODIS/MCD12Q1.061
44. Dauby, G., Zaiss, R., Blach-Overgaard, A., Catarino, L., Damen, T., Deblauwe, V., Dessein, S., Dransfield, J., Droissart, V., Duarte, M. C., Engledow, H., Fadeur, G., Figueira, R., Gereau, R. E., Hardy, O. J., Harris, D. J., de Heij, J., Janssens, S., Klomberg, Y., Ley, A. C., Mackinder, B. A., Meerts, P., van de Poel, J. L., Sonké B, B., Sosef, M. S., Stévart, T., Stoffelen, P., Svenning, J. C., Sepulchre, P., van der Burgt, X., Wieringa, J. J., & Couvreur, T. L. 2016. RAINBIO: A mega-database of tropical African vascular plants distributions. PhytoKeys, (74), 1.
45. Maass J M, Jaramillo V, Martínez-Yrízar A, Guillermo Ibarra-Manríquez. Aspectos funcionales del ecosistema de selva baja caducifolia en Chamela, Jalisco. Historia natural de Chamela, 2002: 525-542.
46. Méndez‐Toribio, M., Meave, J. A., Zermeño‐Hernández, I., & Guillermo Ibarra-Manríquez. Effects of slope aspect and topographic position on environmental variables, disturbance regime and tree community attributes in a

seasonal tropical dry forest. Journal of Vegetation Science, 2016, 27(6): 1094-1103.
47. Madhumali, R., Wahala, W., Sanjeewani, H. K. N., De Costa, W. 2023. Influence of Geographical Aspect and Topography on Canopy Openness in Tropical Rainforests of Sri Lanka along an Altitudinal Gradient. bioRxiv, 2023: 2023.07. 06.547768.
48. Savage, J. C., & Plafker, G. 1991. Tide gage measurements of uplift along the south coast of Alaska. Journal of Geophysical Research: Solid Earth, 96(B3), 4325-4335.
49. Spear, R. W., Davis, M. B., & Shane, L. C. 1994. Late Quaternary history of low‐and mid‐elevation vegetation in the White Mountains of New Hampshire. Ecological Monographs, 64(1), 85-109.
50. Woodwell, G. M., & Whittaker, R. H. 1968. Primary production in terrestrial ecosystems. American Zoologist, 8(1): 19-30.
51. Campioli, M., Vicca, S., Luyssaert, S., Bilcke, J., Ceschia, E., Chapin Iii, F. S., Ciais, P., Fernández-Martínez, M., Malhi, Y., Obersteiner, M., Olefeldt, D., Papale, D., Piao, S. L., Peñuelas, J., Sullivan, P. F., Wang, X., Zenone, T., & Janssens, I. A. 2015. Biomass production efficiency controlled by management in temperate and boreal ecosystems. Nature Geoscience, 8(11): 843-846.
52. Li, D., Niu, S., & Luo, Y. 2012. Global patterns of the dynamics of soil carbon and nitrogen stocks following afforestation: A meta-analysis. New Phytologist, 195(1): 172-181.
53. Wang, F., Ding, Y., Sayer, E. J., Li, Q., Zou, B., Mo, Q., Li, Y., Lu, X., Tang, J., Zhu, W., & Li, Z. 2017. Tropical forest restoration: Fast resilience of plant biomass contrasts with slow recovery of stable soil c stocks. Functional Ecology, 31(12): 2344-2355.
54. Chen, X., Maignan, F., Viovy, N., Bastos, A., Goll, D., Wu, J., Liu, L., Yue, C., Peng, S., Yuan, W., da Conceição, A. C., O'Sullivan, M., & Ciais, P. 2020. Novel representation of leaf phenology improves simulation of Amazonian evergreen forest photosynthesis in a land surface model. Journal of Advances in Modeling Earth Systems, 12(1): e2018MS001565.

55. Green, J., Berry, J., Ciais, P., Zhang, Y., & Gentine, P. 2020. Amazon rainforest photosynthesis increases in response to atmospheric dryness. Science Advances, 6(47): eabb7232.
56. Li, Q., Chen, X., Yuan, W., Lu, H., Shen, R., Wu, S., Gong, F., Dai, Y., Liu, L., Sun, Q., Zhang, C., & Su, Y. 2021. Remote sensing of seasonal climatic constraints on leaf phenology across pantropical evergreen forest biome. Earth's Future, 9(9): e2021EF002160.
57. Chen, X., Ciais, P., Maignan, F., Zhang, Y., Bastos, A., Liu, L., Bacour, C. d., Fan, L., Gentine, P., Goll, D., Green, J., Kim, H., Li, L., Liu, Y., Peng, S., Tang, H., Viovy, N., Wigneron, J.-P., Wu, J., Yuan, W., & Zhang, H. 2021. Vapor pressure deficit and sunlight explain seasonality of leaf phenology and photosynthesis across Amazonian evergreen broadleaved forest. Global Biogeochemical Cycles, 35(6): e2020GB006893.
58. Yang, X., Wu, J., Chen, X., Ciais, P., Maignan, F., Yuan, W., Piao, S., Yang, S., Gong, F., & Su, Y. 2021. A comprehensive framework for seasonal controls of leaf abscission and productivity in evergreen broadleaved tropical and subtropical forests. The Innovation, 2(4).
59. Peñuelas, J., Ciais, P., Canadell, J. G., Janssens, I. A., Fernández-Martínez, M., Carnicer, J., Obersteiner, M., Piao, S., Vautard, R., & Sardans, J. 2017. Shifting from a fertilization-dominated to a warming-dominated period. Nature Ecology & Evolution, 1(10): 1438-1445.
60. Cuni-Sanchez, A., Sullivan, M. J. P., Platts, P. J., Lewis, S. L., Marchant, R., Imani, G. r., Hubau, W., Abiem, I., Adhikari, H., Albrecht, T., Altman, J., Amani, C., Aneseyee, A. B., Avitabile, V., Banin, L., Batumike, R., Bauters, M., Beeckman, H., Begne, S. K., Bennett, A. C., Bitariho, R., Boeckx, P., Bogaert, J., BrĂ¤uning, A., Bulonvu, F., Burgess, N. D., Calders, K., Chapman, C., Chapman, H., Comiskey, J., de Haulleville, T., Decuyper, M., DeVries, B., Dolezal, J., Droissart, V., Ewango, C., Feyera, S., Gebrekirstos, A., Gereau, R., Gilpin, M., Hakizimana, D., Hall, J., Hamilton, A., Hardy, O., Hart, T., Heiskanen, J., Hemp, A., Herold, M.,

Hiltner, U., Horak, D., Kamdem, M.-N., Kayijamahe, C., Kenfack, D., Kinyanjui, M. J., Klein, J., Lisingo, J., Lovett, J., Lung, M., Makana, J.-R., Malhi, Y., Marshall, A., Martin, E. H., Mitchard, E. T. A., Morel, A., Mukendi, J. T., Muller, T., Nchu, F., Nyirambangutse, B., Okello, J., Peh, K. S. H., Pellikka, P., Phillips, O. L., Plumptre, A., Qie, L., Rovero, F., Sainge, M. N., Schmitt, C. B., Sedlacek, O., Ngute, A. S. K., Sheil, D., Sheleme, D., Simegn, T. Y., Simo-Droissart, M., Sonké, B., Soromessa, T., Sunderland, T., Svoboda, M., Taedoumg, H., Taplin, J., Taylor, D., Thomas, S. C., Timberlake, J., Tuagben, D., Umunay, P., Uzabaho, E., Verbeeck, H., Vleminckx, J., Wallin, G. r., Wheeler, C., Willcock, S., Woods, J. T., & Zibera, E. 2021. High aboveground carbon stock of african tropical montane forests. Nature, 596(7873): 536-542.

61. Zeng, Z., Estes, L., Ziegler, A. D., Chen, A., Searchinger, T., Hua, F., Guan, K., Jintrawet, A., & F. Wood, E. 2018. Highland cropland expansion and forest loss in Southeast Asia in the twenty-first century. Nature Geoscience, 11(8), 556-562.
62. Alexandratos, N., & Bruinsma, J. 2012. World agriculture towards 2030/2050: the 2012 revision.
63. Malhi, Y., Girardin, C. c. A. J., Goldsmith, G. R., Doughty, C. E., Salinas, N., Metcalfe, D. B., Huaraca Huasco, W., Silva-Espejo, J. E., del Aguilla-Pasquell, J., Farfán Amézquita, F., Aragão, L. E. O. C., Guerrieri, R., Ishida, F. o. Y., Bahar, N. H. A., Farfan-Rios, W., Phillips, O. L., Meir, P., & Silman, M. 2017. The variation of productivity and its allocation along a tropical elevation gradient: A whole carbon budget perspective. New Phytologist, 214(3): 1019-1032.
64. Besnard, S., Koirala, S., Santoro, M., Weber, U., Nelson, J., Gütter, J., Herault, B., Kassi, J., N'Guessan, A., Neigh, C., Poulter, B., Zhang, T., and Carvalhais, N.: Mapping global forest age from forest inventories, biomass and climate data, Earth Syst. Sci. Data, 13, 4881–4896, https://doi.org/10.5194/essd-13-4881-2021, 2021.
65. Sierra Cornejo, N., Leuschner, C., Becker, J. N., Hemp, A., Schellenberger Costa, D., & Hertel, D. 2021. Climate implications on forest above-and belowground carbon allocation patterns along a tropical elevation gradient on MT. Kilimanjaro

(Tanzania). Oecologia, 195: 797-812.

66. Peddinti, S. R., Kambhammettu, B., Rodda, S. R., Thumaty, K. C., & Suradhaniwar, S. 2020. Dynamics of ecosystem water use efficiency in Citrus Orchards of Central India using Eddy covariance and landsat measurements. Ecosystems, 23: 511-528.

67. Sullivan, M. J. P., Lewis, S. L., Affum-Baffoe, K., Castilho, C., Costa, F. v., Sanchez, A. C., Ewango, C. E. N., Hubau, W., Marimon, B., Monteagudo-Mendoza, A., Qie, L., Sonké, B., Martinez, R. V., Baker, T. R., Brienen, R. J. W., Feldpausch, T. R., Galbraith, D., Gloor, M., Malhi, Y., Aiba, S.-I., Alexiades, M. N., Almeida, E. C., de Oliveira, E. A., Dávila, E. Á. l., Loayza, P. A., Andrade, A., Vieira, S. A., Aragão, L. E. O. C., Araujo-Murakami, A., Arets, E. J. M. M., Arroyo, L., Ashton, P., Aymard C, G., Baccaro, F. c. B., Banin, L. F., Baraloto, C., Camargo, P. n. B., Barlow, J., Barroso, J., Bastin, J.-F. o., Batterman, S. A., Beeckman, H., Begne, S. K., Bennett, A. C., Berenguer, E., Berry, N., Blanc, L., Boeckx, P., Bogaert, J., Bonal, D., Bongers, F., Bradford, M., Brearley, F. Q., Brncic, T., Brown, F., Burban, B., Camargo, J. L. s., Castro, W., Céron, C., Ribeiro, S. C., Moscoso, V. C., Chave, J. m., Chezeaux, E., Clark, C. J., de Souza, F. C., Collins, M., Comiskey, J. A., Valverde, F. C., Medina, M. C., da Costa, L., Dančák, M., Dargie, G. C., Davies, S., Cardozo, N. D., de Haulleville, T., de Medeiros, M. B., del Aguila Pasquel, J., Derroire, G. r., Di Fiore, A., Doucet, J.-L., Dourdain, A. l., Droissart, V., Duque, L. F., Ekoungoulou, R., Elias, F., Erwin, T., Esquivel-Muelbert, A., Fauset, S., Ferreira, J., Llampazo, G. F., Foli, E., Ford, A., Gilpin, M., Hall, J. S., Hamer, K. C., Hamilton, A. C., Harris, D. J., Hart, T. B., Hédl, R., Herault, B., Herrera, R., Higuchi, N., Hladik, A., Coronado, E. d. H., Huamantupa-Chuquimaco, I., Huasco, W. H., Jeffery, K. J., Jimenez-Rojas, E., Kalamandeen, M., Djuikouo, M. N. l. K., Kearsley, E., Umetsu, R. K., Kho, L. K., Killeen, T., Kitayama, K., Klitgaard, B., Koch, A., Labrière, N., Laurance, W., Laurance, S., Leal, M. E., Levesley, A., Lima, A. J. N., Lisingo, J., Lopes, A. P., Lopez-Gonzalez, G., Lovejoy, T., Lovett, J. C., Lowe, R., Magnusson, W. E., Malumbres-Olarte, J., Manzatto, Ă. n. G., Marimon, B. H., Marshall, A. R., Marthews, T., de Almeida Reis, S. M., Maycock, C.,

Melgaço, K., Mendoza, C., Metali, F., Mihindou, V., Milliken, W., Mitchard, E. T. A., Morandi, P. S., Mossman, H. L., Nagy, L., Nascimento, H., Neill, D., Nilus, R., Vargas, P. N. e., Palacios, W., Camacho, N. P., Peacock, J., Pendry, C., Peñuela Mora, M. C., Pickavance, G. C., Pipoly, J., Pitman, N., Playfair, M., Poorter, L., Poulsen, J. R., Poulsen, A. D., Preziosi, R., Prieto, A., Primack, R. B., RamĂ-rez-Angulo, H., Reitsma, J., Réjou-Méchain, M., Correa, Z. R., de Sousa, T. R., Bayona, L. R., Roopsind, A., Rudas, A. n., Rutishauser, E., Abu Salim, K., SalomĂŁo, R. P., Schietti, J., Sheil, D., Silva, R. C., Espejo, J. S., Valeria, C. S., Silveira, M., Simo-Droissart, M., Simon, M. F., Singh, J., Soto Shareva, Y. C., Stahl, C., Stropp, J., Sukri, R., Sunderland, T., SvÁtek, M., Swaine, M. D., Swamy, V., Taedoumg, H., Talbot, J., Taplin, J., Taylor, D., ter Steege, H., Terborgh, J., Thomas, R., Thomas, S. C., Torres-Lezama, A., Umunay, P., Gamarra, L. V., van der Heijden, G., van der Hout, P., van der Meer, P., van Nieuwstadt, M., Verbeeck, H., Vernimmen, R., Vicentini, A., Vieira, I. C. l. G., Torre, E. V., Vleminckx, J., Vos, V., Wang, O., White, L. J. T., Willcock, S., Woods, J. T., Wortel, V., Young, K., Zagt, R., Zemagho, L., Zuidema, P. A., Zwerts, J. A., & Phillips, O. L. 2020. Long-term thermal sensitivity of Earth's tropical forests. Science, 368(6493): 869-874.

68. Hubau, W., Lewis, S. L., Phillips, O. L., Affum-Baffoe, K., Beeckman, H., Cuní-Sanchez, A., Daniels, A. K., Ewango, C. E. N., Fauset, S., Mukinzi, J. M., Sheil, D., Sonké., Sullivan, M. J. P., Sunderland, T. C. H., Taedoumg, H., Thomas, S. C., White, L. J. T., Abernethy, K. A., Adu-Bredu, S., Amani, C. A., Baker, T. R., Banin, L. F., Baya, F. l., Begne, S. K., Bennett, A. C., Benedet, F., Bitariho, R., Bocko, Y. E., Boeckx, P., Boundja, P., Brienen, R. J. W., Brncic, T., Chezeaux, E., Chuyong, G. B., Clark, C. J., Collins, M., Comiskey, J. A., Coomes, D. A., Dargie, G. C., de Haulleville, T., Kamdem, M. N. D., Doucet, J.-L., Esquivel-Muelbert, A., Feldpausch, T. R., Fofanah, A., Foli, E. G., Gilpin, M., Gloor, E., Gonmadje, C., Gourlet-Fleury, S., Hall, J. S., Hamilton, A. C., Harris, D. J., Hart, T. B., Hockemba, M. B. N., Hladik, A., Ifo, S. A., Jeffery, K. J., Jucker, T., Yakusu, E. K., Kearsley, E., Kenfack, D., Koch, A., Leal, M. E., Levesley, A., Lindsell, J. A., Lisingo, J.,

Lopez-Gonzalez, G., Lovett, J. C., Makana, J.-R., Malhi, Y., Marshall, A. R., Martin, J., Martin, E. H., Mbayu, F. M., Medjibe, V. P., Mihindou, V., Mitchard, E. T. A., Moore, S., Munishi, P. K. T., Bengone, N. N., Ojo, L., Ondo, F. l. E., Peh, K. S. H., Pickavance, G. C., Poulsen, A. D., Poulsen, J. R., Qie, L., Reitsma, J., Rovero, F., Swaine, M. D., Talbot, J., Taplin, J., Taylor, D. M., Thomas, D. W., Toirambe, B., Mukendi, J. T., Tuagben, D., Umunay, P. M., van der Heijden, G. M. F., Verbeeck, H., Vleminckx, J., Willcock, S., Wöll, H. r., Woods, J. T., & Zemagho, L. 2020. Asynchronous carbon sink saturation in African and Amazonian tropical forests. Nature, 579(7797): 80-87.

69. Sippel, S., Reichstein, M., Ma, X., Mahecha, M. D., Lange, H., Flach, M., & Frank, D. 2018. Drought, heat, and the carbon cycle: A review. Current Climate Change Reports, 4: 266-286.
70. Williams, C. A. 2014. Heat and drought extremes likely to stress ecosystem productivity equally or more in a warmer, co2 rich future. Environmental Research Letters, 9(10): 101002.
71. Williams, I., Torn, M., Riley, W., & Wehner, M. 2014. Impacts of climate extremes on gross primary production under global warming. Environmental Research Letters, 9(9): 094011.
72. Cubasch, U., Meehl, G., Boer, G., Stouffer, R., Dix, M., Noda, A., Senior, C., Raper, S., & Yap, K. (2001). Projections of future climate change. In Climate change 2001: The scientific basis. Contribution of WG1 to the third assessment report of the IPCC (TAR) (pp. 525-582): Cambridge University Press.
73. Zscheischler, J., Westra, S., van den Hurk, B. J. J. M., Seneviratne, S. I., Ward, P. J., Pitman, A., AghaKouchak, A., Bresch, D. N., Leonard, M., Wahl, T., & Zhang, X. 2018. Future climate risk from compound events. Nature Climate Change, 8(6): 469-477.
74. Duque, A., Peña, M. A., Cuesta, F., González-Caro, S., Kennedy, P., Phillips, O. L., Calderón-Loor, M., Blundo, C., Carilla, J., Cayola, L., Farfán-Ríos, W., Fuentes, A., Grau, R., Homeier, J., Loza-Rivera, M. I., Malhi, Y., Malizia, A., Malizia, L.,

Martínez-Villa, J. A., Myers, J. A., Osinaga-Acosta, O., Peralvo, M., Pinto, E., Saatchi, S., Silman, M., Tello, J. S., Terán-Valdez, A., & Feeley, K. J. 2021. Mature Andean forests as globally important carbon sinks and future carbon refuges. Nature Communications, 2021, 12(1): 2138.

75. Van Zyl, J. J. 2001. The Shuttle Radar Topography Mission (SRTM): A breakthrough in remote sensing of topography. Acta astronautica, 48(5-12): 559-565.
76. Saatchi, S. S., Harris, N. L., Brown, S., Lefsky, M., Mitchard, E. T. A., Salas, W., Zutta, B. R., Buermann, W., Lewis, S. L., Hagen, S., Petrova, S., White, L., Silman, M., & Morel, A. 2011. Benchmark map of forest carbon stocks in tropical regions across three continents. Proceedings of the National Academy of Sciences, 108(24): 9899-9904.
77. Eggleston, H., Buendia, L., Miwa, K., Ngara, T., & Tanabe, K. 2006. 2006 IPCC guidelines for national greenhouse gas inventories.
78. Ye, J., Yue, C., Hu, Y., & Ma, H. 2021. Spatial patterns of global-scale forest root-shoot ratio and their controlling factors. Science of The Total Environment, 800: 149251.
79. Alicia, L., Keryn, I. P., David, F. R. P. B., John, J. E., Craig, B., Michael, B., Kim, B., Jennifer, C., Tron Haakon, E., Jacqueline, R. E., Anthony, F., Justin, J., Maurizio, M., Kelvin, D. M., Gregorio, M., Wilson Ancelm, M., Elizabeth, P., Stephen, R., Casey, M. R., Ricardo, R.-P., Stan, S., Alison, S., Daniel, W., Christian, W., Ayalsew, Z., & Jérôme, C. 2018. Tree size and climatic water deficit control root to shoot ratio in individual trees globally. The New Phytologist, 217(1): 8-11.
80. Hertel, D., Moser, G., Culmsee, H., Erasmi, S., Horna, V., Schuldt, B., & Leuschner, C. 2009. Below-and above-ground biomass and net primary production in a paleotropical natural forest (Sulawesi, Indonesia) as compared to neotropical forests. Forest ecology and management, 258(9): 1904-1912.
81. Kenzo, T., Ichie, T., Hattori, D., Itioka, T., Handa, C., Ohkubo, T., Kendawang, J. J., Nakamura, M., Sakaguchi, M., Takahashi, N., Okamoto, M., Tanaka-Oda, A.,

Sakurai, K., & Ninomiya, I. 2009. Development of allometric relationships for accurate estimation of above- and below-ground biomass in tropical secondary forests in Sarawak, Malaysia. Journal of Tropical Ecology, 25(4): 371-386.

82. Feng, Y., Zeng, Z., Searchinger, T. D., Ziegler, A. D., Wu, J., Wang, D., He, X., Elsen, P. R., Ciais, P., Xu, R., Guo, Z., Peng, L., Tao, Y., Spracklen, D. V., Holden, J., Liu, X., Zheng, Y., Xu, P., Chen, J., Jiang, X., Song, X.-P., Lakshmi, V., Wood, E. F., & Zheng, C. 2022. Doubling of annual forest carbon loss over the tropics during the early twenty-first century. Nature Sustainability, 5(5): 444-451.
83. Uribe, M. d. R., Coe, M. T., Castanho, A. D., Macedo, M. N., Valle, D., & Brando, P. M. 2023. Net loss of biomass predicted for tropical biomes in a changing climate. Nature Climate Change, 13(3): 274-281.
84. Yang, Y., Shi, Y., Sun, W., Chang, J., Zhu, J., Chen, L., Wang, X., Guo, Y., Zhang, H., Yu, L., Zhao, S., Xu, K., Zhu, J., Shen, H., Wang, Y., Peng, Y., Zhao, X., Wang, X., Hu, H., Chen, S., Huang, M., Wen, X., Wang, S., Zhu, B., Niu, S., Tang, Z., Liu, L., & Fang, J. 2022. Terrestrial carbon sinks in china and around the world and their contribution to carbon neutrality. Science China Life Sciences, 65(5): 861-895.
85. Pongratz, J., Schwingshackl, C., Bultan, S., Obermeier, W., Havermann, F., & Guo, S. 2021. Land use effects on climate: Current state, recent progress, and emerging topics. Current Climate Change Reports: 1-22.
86. Smith, C. C., Healey, J. R., Berenguer, E., Young, P. J., Taylor, B., Elias, F., Espírito-Santo, F., & Barlow, J. 2021. Old-growth forest loss and secondary forest recovery across amazonian countries. Environmental Research Letters, 16(8): 085009.
87. Silva, C. V. J., Aragão, L. E. O. C., Young, P. J., Espirito-Santo, F., Berenguer, E., Anderson, L. O., Brasil, I., Pontes-Lopes, A., Ferreira, J., Withey, K., França, F., Graça, P. M. L. A., Kirsten, L., Xaud, H., Salimon, C., Scaranello, M. A., Castro, B., Seixas, M., Farias, R., & Barlow, J. 2020. Estimating the multi-decadal carbon deficit of burned amazonian forests. Environmental Research Letters, 15(11):

114023.

88. Crouzeilles, R., Beyer, H. L., Monteiro, L. M., Feltran-Barbieri, R., PessĂ´a, A. C. M., Barros, F. S. M., Lindenmayer, D. B., Lino, E. D. S. M., Grelle, C. E. V., Chazdon, R. L., Matsumoto, M., Rosa, M., Latawiec, A. E., & Strassburg, B. B. N. 2020. Achieving cost-effective landscape-scale forest restoration through targeted natural regeneration. Conservation Letters, 13(3): e12709.
89. Lang, N., Jetz, W., Schindler, K., & Wegner, J. D. 2023. A high-resolution canopy height model of the earth. Nature Ecology & Evolution: 1-12.
90. Wang, S., Zhou, L., Chen, J., Ju, W., Feng, X., & Wu, W. 2011. Relationships between net primary productivity and stand age for several forest types and their influence on China's carbon balance. Journal of environmental management, 92(6): 1651-1662.
91. Chen, J. M., Mo, G., Pisek, J., Liu, J., Deng, F., Ishizawa, M., & Chan, D. 2012. Effects of foliage clumping on the estimation of global terrestrial gross primary productivity. Global biogeochemical cycles, 26(1).
92. Hu, Z., Shi, H., Cheng, K., Wang, Y. P., Piao, S., Li, Y., Zhang, L., Xia, J., Zhou, L., Yuan, W., Running, S., Li, L., Hao, Y., He, N., Yu, Q., & Yu, G. 2018. Joint structural and physiological control on the interannual variation in productivity in a temperate grassland: A data‐model comparison. Global change biology, 24(7), 2965-2979.
93. Yu, W., Li, J., Liu, Q., Yin, G., Zeng, Y., Lin, S., & Zhao, J. 2020. A simulation-based analysis of topographic effects on LAI inversion over sloped terrain. IEEE Journal of Selected Topics in Applied Earth Observations and Remote Sensing, 13, 794-806.
94. Liu, Y., Xiao, J., Ju, W., Zhu, G., Wu, X., Fan, W., Li, D., & Zhou, Y. 2018. Satellite-derived LAI products exhibit large discrepancies and can lead to substantial uncertainty in simulated carbon and water fluxes. Remote Sensing of Environment, 206, 174-188.
95. Xing, X., Wu, M., Zhang, W., Ju, W., Tagesson, T., He, W., Wang, S., Wang, J., Hu,

L., Yuan, S., Zhu, T., Wang, X., Ran, Y., Li, S., Wang, C., & Jiang, F. 2023. Modeling China's terrestrial ecosystem gross primary productivity with BEPS model: Parameter sensitivity analysis and model calibration. Agricultural and Forest Meteorology, 343, 109789.

96. Migliavacca, M., Musavi, T., Mahecha, M. D., Nelson, J. A., Knauer, J., Baldocchi, D. D., Perez-Priego, O., Christiansen, R., Peters, J., Anderson, K., Bahn, M., Black, T. A., Blanken, P. D., Bonal, D., Buchmann, N., Caldararu, S., Carrara, A., Carvalhais, N., Cescatti, A., Chen, J., Cleverly, J., Cremonese, E., Desai, A. R., El-Madany, T. S., Farella, M. M., Fernández-Martínez, M., Filippa, G., Forkel, M., Galvagno, M., Gomarasca, U., Gough, C. M., Göckede, M., Ibrom, A., Ikawa, H., Janssens, I. A., Jung, M., Kattge, J., Keenan, T. F., Knohl, A., Kobayashi, H., Kraemer, G., Law, B. E., Liddell, M. J., Ma, X., Mammarella, I., Martini, D., Macfarlane, C., Matteucci, G., Montagnani, L., Pabon-Moreno, D. E., Panigada, C., Papale, D., Pendall, E., Penuelas, J., Phillips, R. P., Reich, P. B., Rossini, M., Rotenberg, E., Scott, R. L., Stahl, C., Weber, U., Wohlfahrt, G., Wolf, S., Wright, I. J., Yakir, D., Zaehle, S., & Reichstein, M. 2021. The three major axes of terrestrial ecosystem function. Nature, 598(7881), 468-472.

97. Abatzoglou, J. T., Dobrowski, S. Z., Parks, S. A., & Hegewisch, K. C. 2018. Terraclimate, a high-resolution global dataset of monthly climate and climatic water balance from 1958-2015. Scientific Data, 5(1): 170191.

98. Chen,Y., Feng, X., & Fu, B. 2021. An improved global remote-sensing-based surface soil moisture (RSSSM) dataset covering 2003–2018. Earth System Science Data, 13(1): 1-31.

99. Ryu, Y., Jiang, C., Kobayashi, H., & Detto, M. 2018. Modis-derived global land products of shortwave radiation and diffuse and total photosynthetically active radiation at 5 km resolution from 2000. Remote Sensing of Environment, 204: 812-825.

100. Zhao, Z., Li, W., Ciais, P., Santoro, M., Cartus, O., Peng, S., Yin, Y., Yue, C., Yang, H., Yu, L., Zhu, L., & Wang, J. 2021. Fire enhances forest degradation within forest

edge zones in Africa. Nature Geoscience, 14(7): 479-483.

101. Muggeo, V. M. R. 2008. Segmented: an R package to fit regression models with broken-line relationships. R news, 8(1): 20-25.

102. He, X., Augusto, L., Goll, D. S., Ringeval, B., Wang, Y., Helfenstein, J., Huang, Y., Yu, K., Wang, Z., Yang, Y., & Hou, E. 2021. Global patterns and drivers of soil total phosphorus concentration. Earth System Science Data, 13(12): 5831-5846.

103. Zhang, C., & Yan, W. Code to support 'Optimal elevations for afforestation and reforestation to enhance biomass carbon accumulation in the tropics'. Zenodo. https://doi.org/10.5281/zenodo.13922571

Table

Table 1 Independent biomass, carbon, and height datasets and corresponding methods to quantify the γ_{rapid} (see **Experimental Procedure** for details).

NO.	Biomass carbon proxies	Biomass carbon data sources	Stand age data sources	Stand age estimation method	γ_{rapid} estimation method	Acronyms
Dataset 1	forest biomass (*in situ*, global)	Smithsonian Institution's Global Forest Carbon (ForC) database [36] and other in-situ datasets[9]		Original stand age records	γ_{rapid} was determined as the slope of linear regression fit between observed forest biomass carbon densities and the stand age of TPRFs where biomass carbon was less than 80% of old-growth forests (stand age ⩾ 100 years) simulated in the Chapman–Richards curve using the space-for-time method.	γ_{rapid}^{GFC}
Dataset 2	Aboveground forest biomass (100m, global, 2018)	ESA-CCI[17]	Cover change map of tropical moisture forest (TMF) (30m, Tropical, 1982-2019)[41] and global plantation years dataset (GPY) (30m, global, 1982-2020)[42]	Stand age of natural regrowth forests was determined based on TMF cover change data. Stand age of planted forests was calculated based on GPY dataset.		$\gamma_{rapid}^{ESA-CCI}$
Dataset 5	Forest canopy height dataset (30m, global, 2019)	GEDI LiDAR dataset[39]				γ_{rapid}^{GEDI}
Dataset 3	Total live woody biomass (0.1°, global, 2000-2019)	Machine-learning (ML)-derived terrestrial live biomass dataset[37]	MODIS MCD12C1 landcover products (0.05°, global, 2001-2019)[43]	Stand age was calculated based on the time series MODIS MCD12C1 land cover dataset.	γ_{rapid} was determined as the slope of linear regression fit between biomass carbon and stand age of TPRFs using the time-series analysis method.	γ_{rapid}^{ML}
Dataset 4	Net ecosystem productivity (0.07273°, global, 1981-2019)	BEPS model[38]				γ_{rapid}^{BEPS}

Figure 1

Click here to access/download;Figure;Fig1.jpg

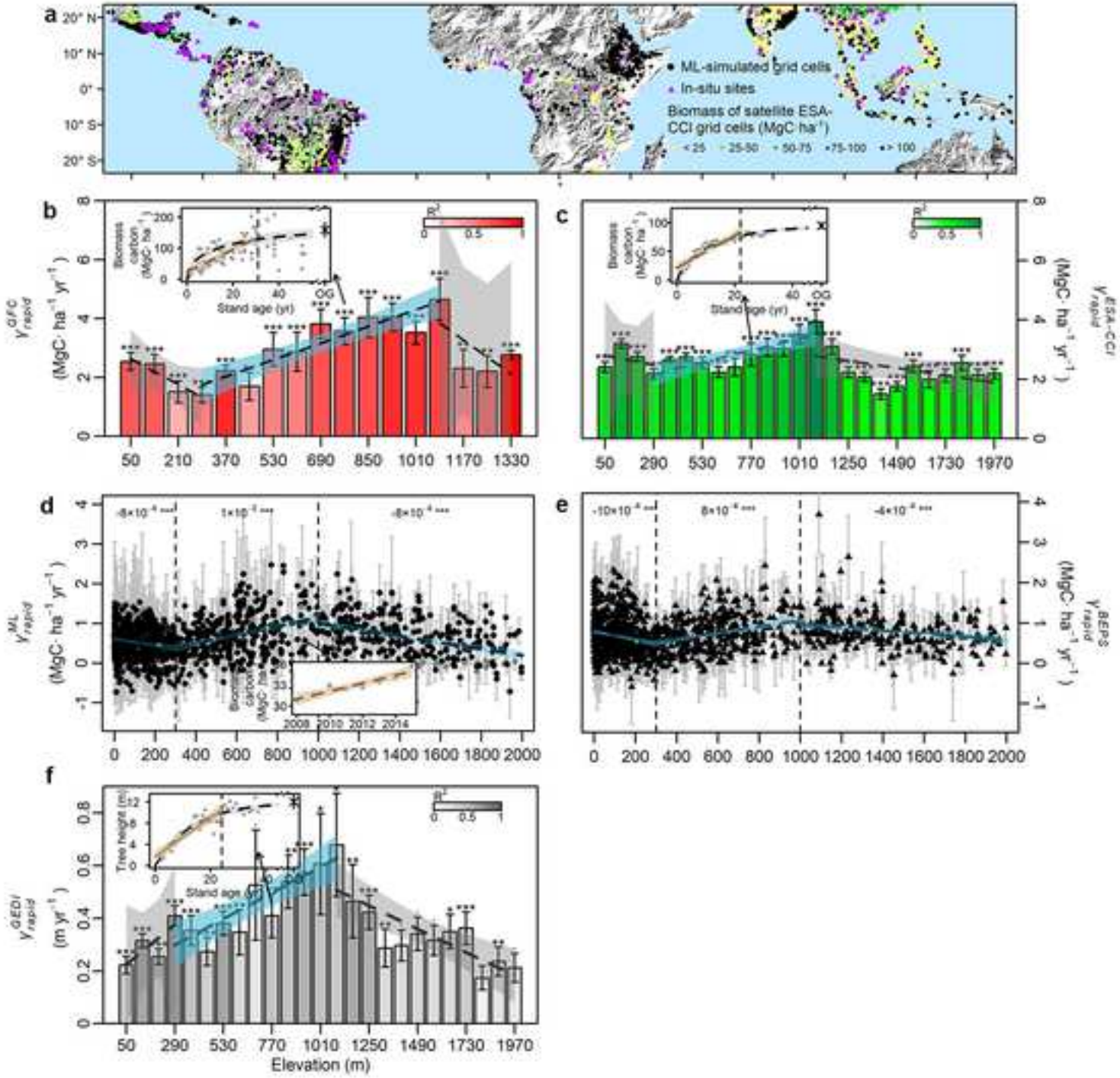

Figure 2

Click here to access/download;Figure;Fig2.jpg

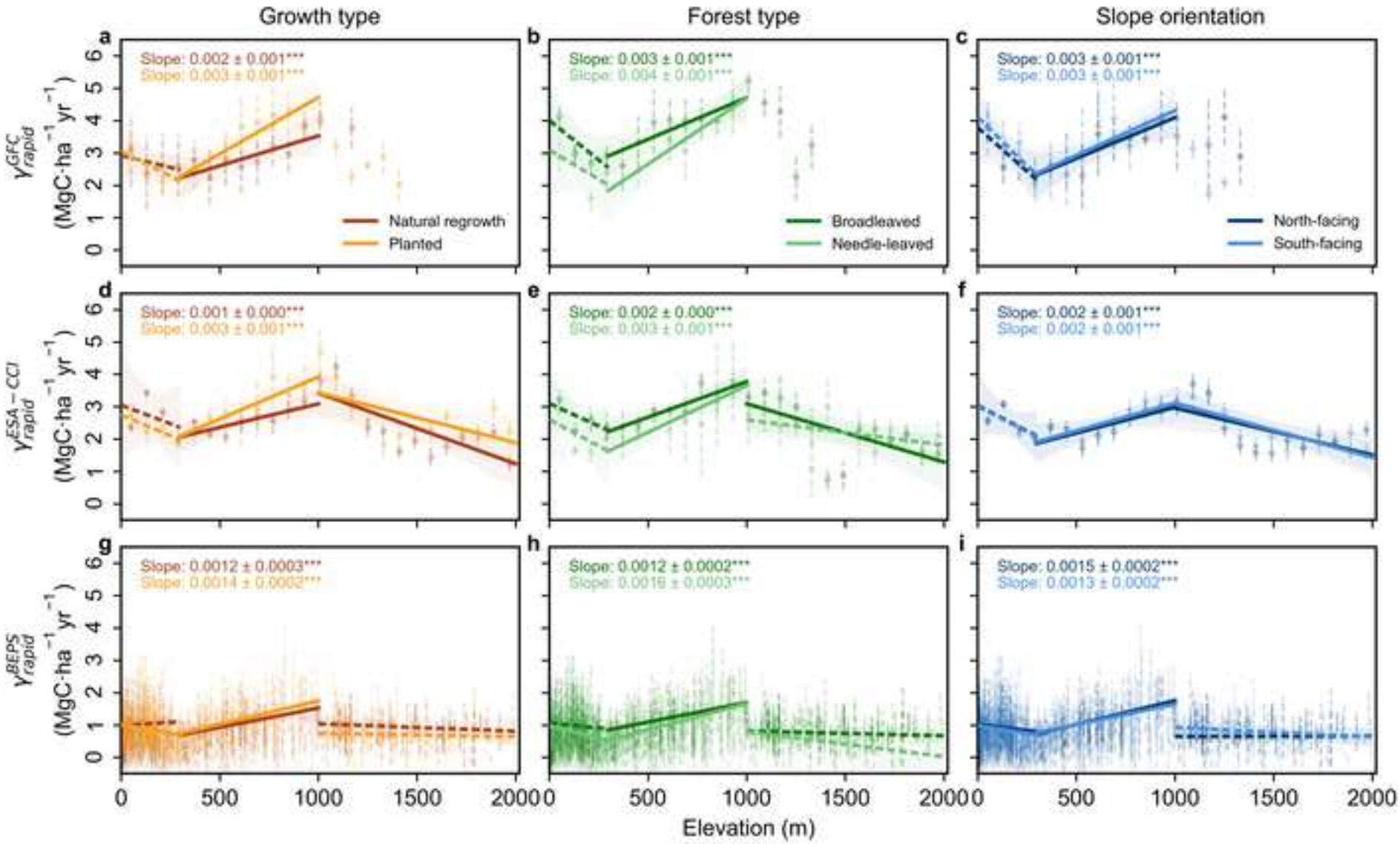

Figure 3

Click here to access/download;Figure;Fig3.jpg

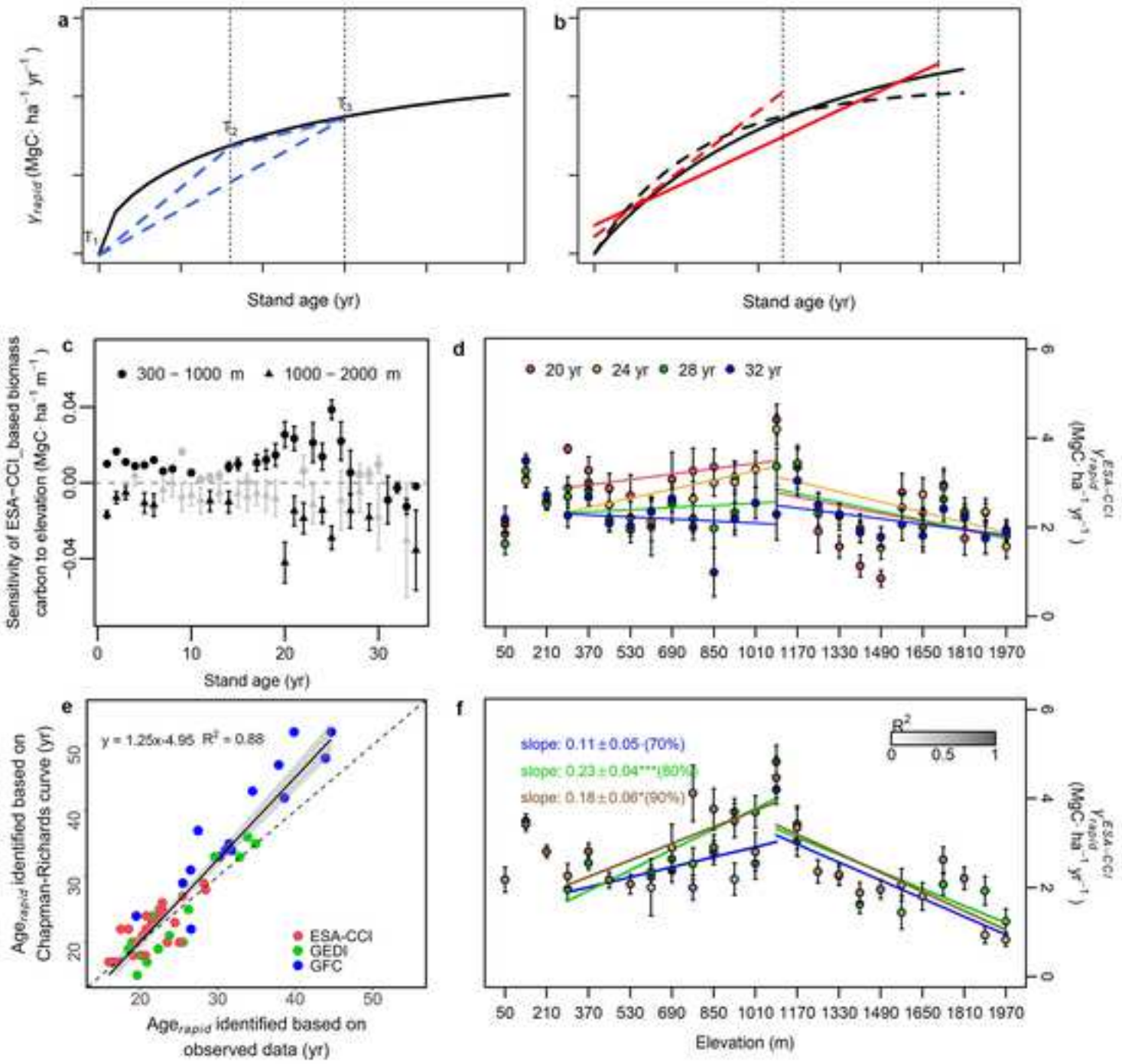

Figure 4

Click here to access/download;Figure;Fig4.jpg

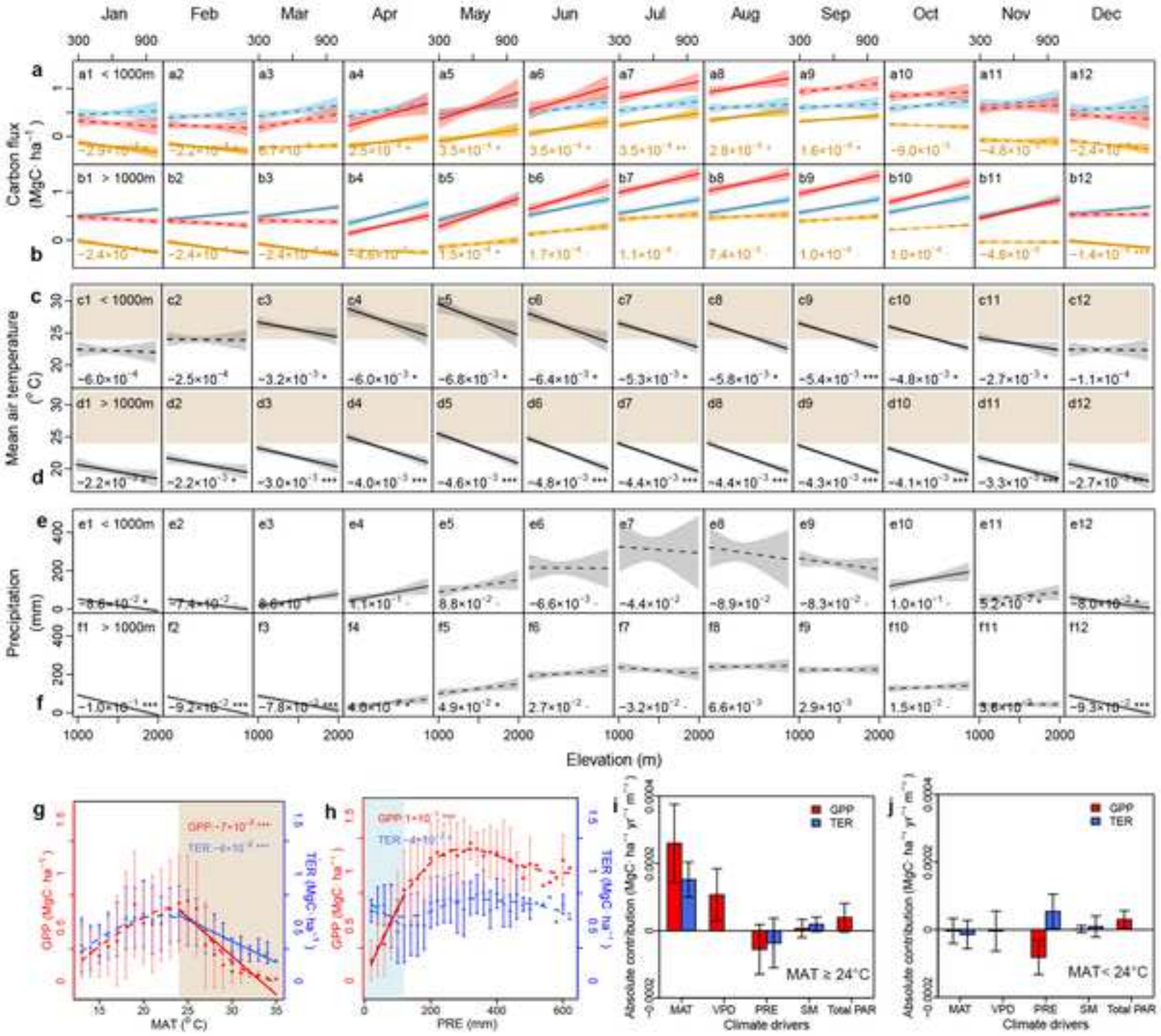

Figure 5

Click here to access/download;Figure;Fig5.jpg

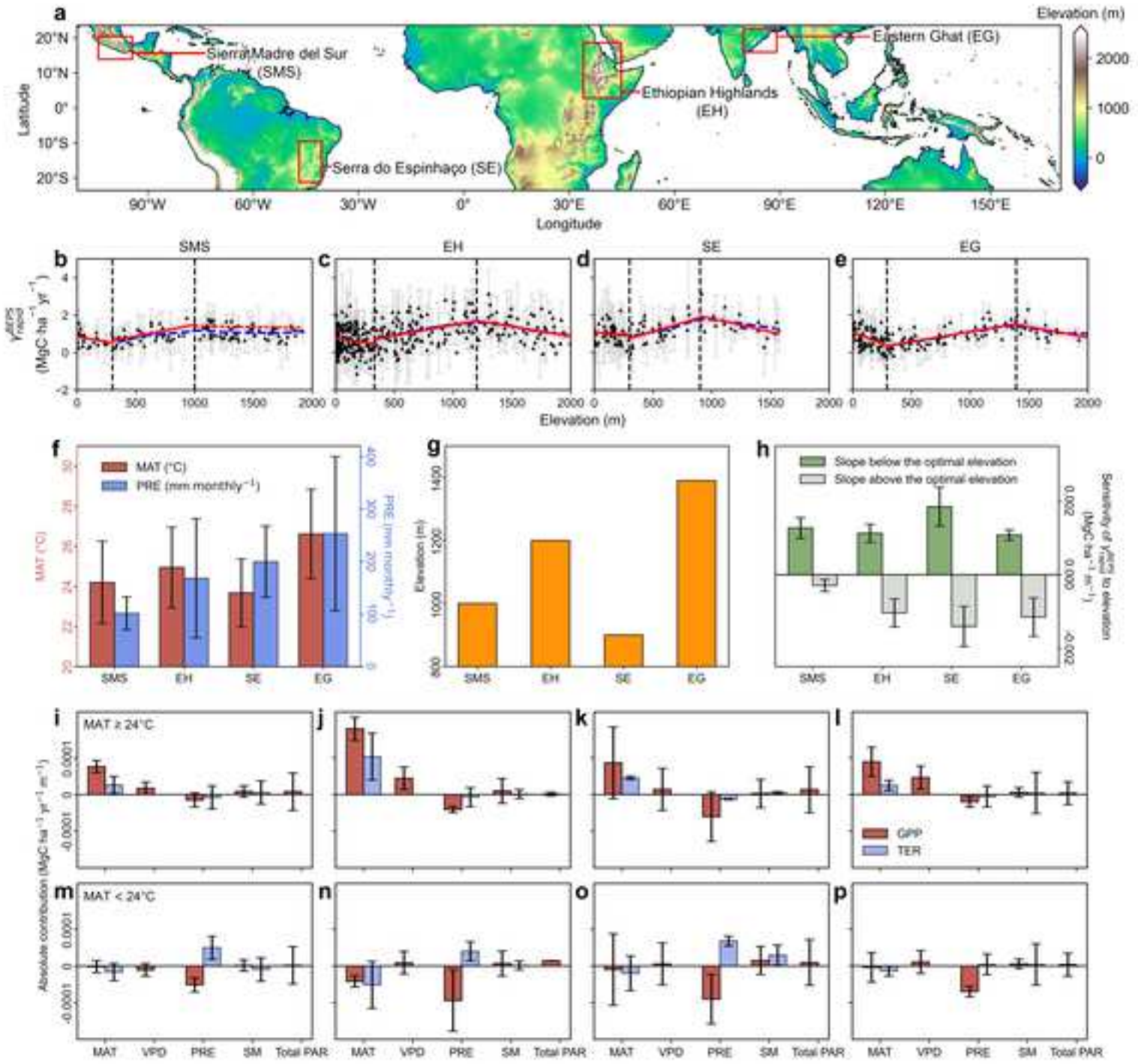

Supplementary information

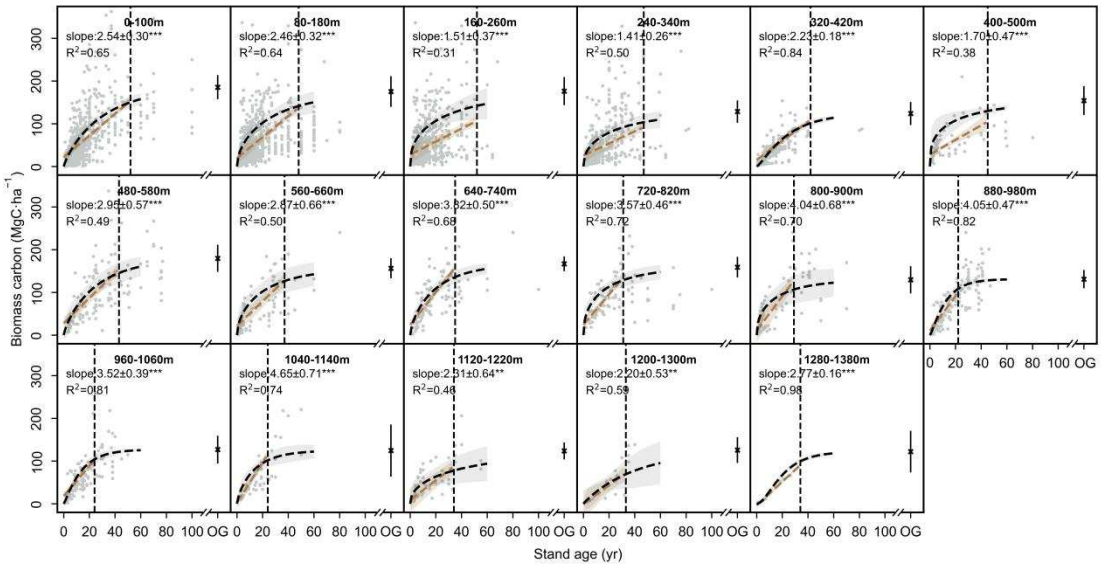

Figure S1. γ_{rapid}^{GFC} for each elevation bin (100±50 m) in 80 m step. Grey points represent *in situ* tree biomass carbon. The Grey dashed curves represent the smoothed trend fitted by Chapman Richards growth model, which was used to find the mature age threshold when the accumulated carbon reached 80% of median carbon of old-growth forest (the black crosses). Error bar indicates one standard error. Brown dashed lines represent the linear regression curves between *in situ* tree biomass carbon and stand age of all sites of TPRFs during the rapid growth stage of trees before approaching maturity within the given elevation bin. Shading represents the 95% confidence interval. Significance of linear regression is indicated in the legend as: • P<0.5, * P<0.1, ** P<0.01, and *** P<0.001.

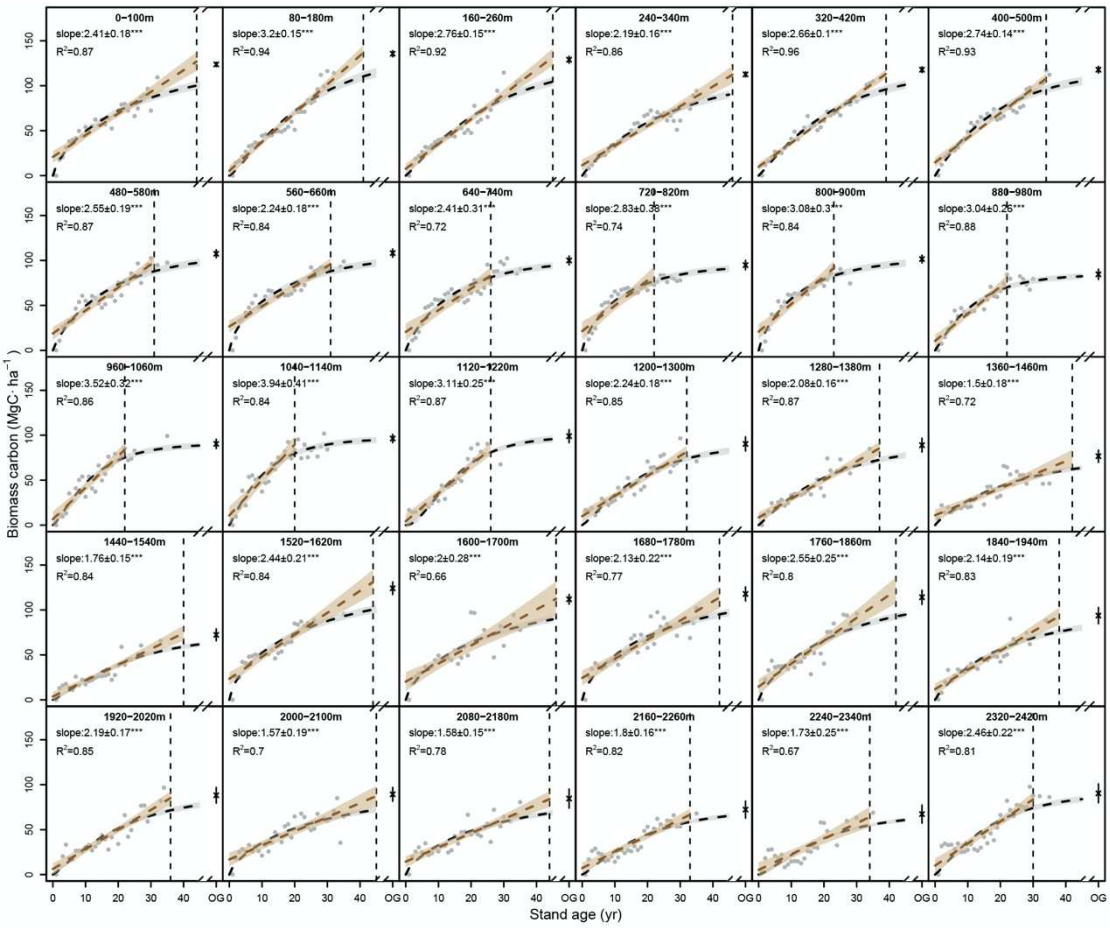

Figure S2. $\gamma_{rapid}^{ESA-CCI}$ for each elevation bin (100±50 m) in 80 m step. Grey points denote the median biomass carbon value calculated for each stand age bin (±1year). Grey dashed curves represent the smoothed trend fitted by Chapman Richards growth model, which was used to find the mature age threshold when the accumulated carbon reached 80% of median carbon of old-growth forest (the black crosses). Error bar indicates one standard error. Brown dashed lines represent the linear regression curves between ESA-CCI-derived total biomass carbon and stand age of all sites of TPRFs during the rapid growth stage of trees before approaching maturity within the given elevation bin. Shading represents the 95% confidence interval. Significance of linear regression is indicated in the legend as: • P<0.5, * P<0.1, **P<0.01, and ***P<0.001.

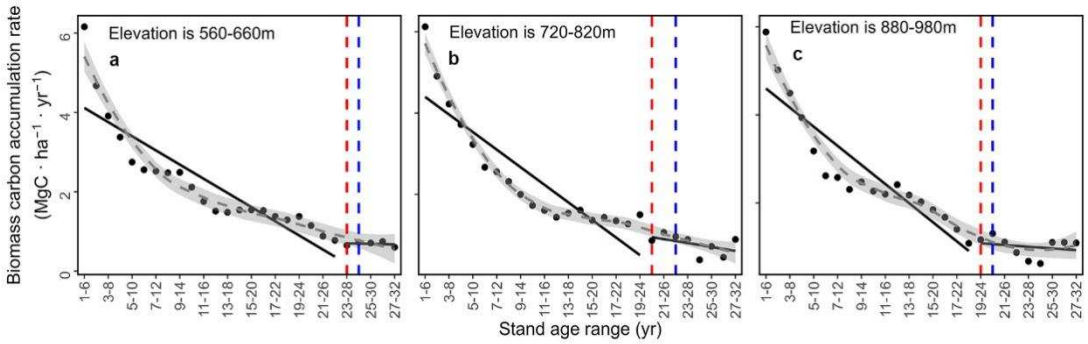

Figure S3. Illustrations for determining the stand age (age_{rapid}) of the rapid growth phase in TPRFs. age_{rapid} was defined as the stand age when there was a break point of the relationship with stand age as stand age increases. Panels **a-c** are examples of age_{rapid} thresholds indentified for three altitude ranges: 560-660 m (**a**), 720-820 m (**b**), and 880-980 m (**c**), respectively, based on ESA-CCI data. The black dots represent the slopes of ordinary least squares regression applied to applied to the relationship between biomass carbon and stand ages for each five-year interval, defining $\gamma_{rapid}^{ESA-CCI}$ for each five years bin. Grey dashed curves and black solid lines represent the smoothed trend fitted by a generalized additive model (GAM) and the linear fits at both sides of each threshold, respectively. The age_{rapid} with an abrupt change between the relationship with stand age as stand age increases was identified using the segmented package in R. Red vertical dashed line represents the observed age_{rapid} indetified using this method. Blue vertical dashed line represents the simulated age_{rapid} identified by 80% of the maximum value on the Chapman–Richards curve.

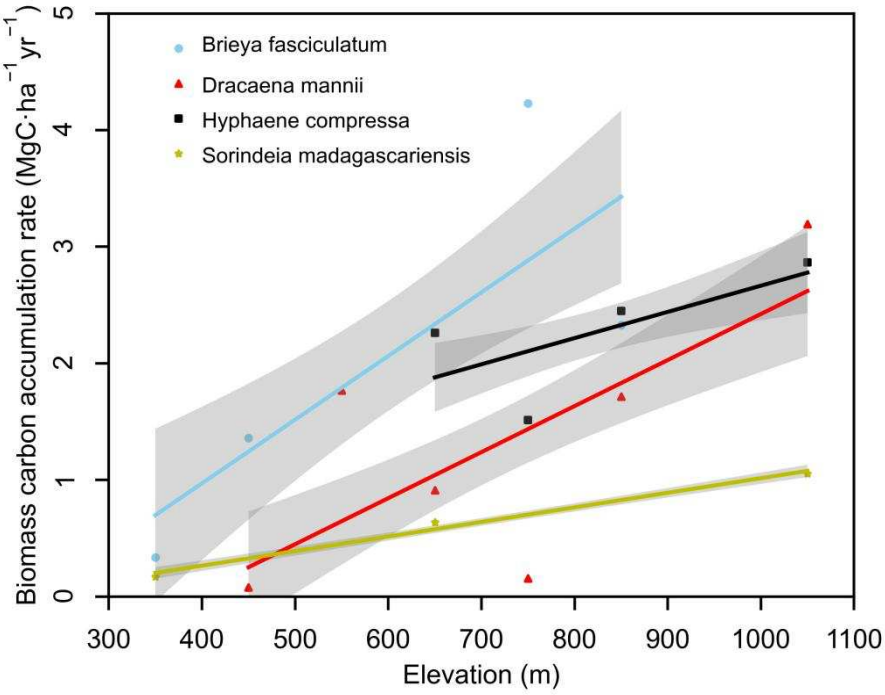

Figure S4. The elevation patterns of $\gamma_{rapid}^{ESA-CCI}$ for four tree species based on a comprehensive mega-database of tropical African vascular plants distributions[2] (Methods).

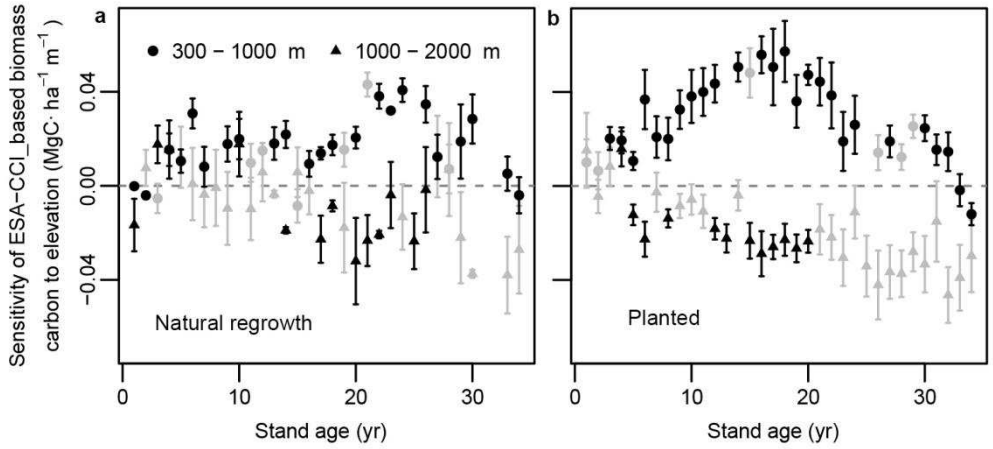

Figure S5. Sensitivity of total biomass carbon derived from ESA-CCI data to elevation (i.e., 300-100 m and 1000-2000 m) across different stand ages for natural regrowth (a) and planted forest (b), respectively. Sensitivity is defined as the slope of the linear regression curve illustrating the relationship between biomass carbon and elevation within each one year stand age bin. Significant relationships ($P \leq 0.05$) are shown in black samples, and non-significant relationships ($P > 0.05$) in grey samples.

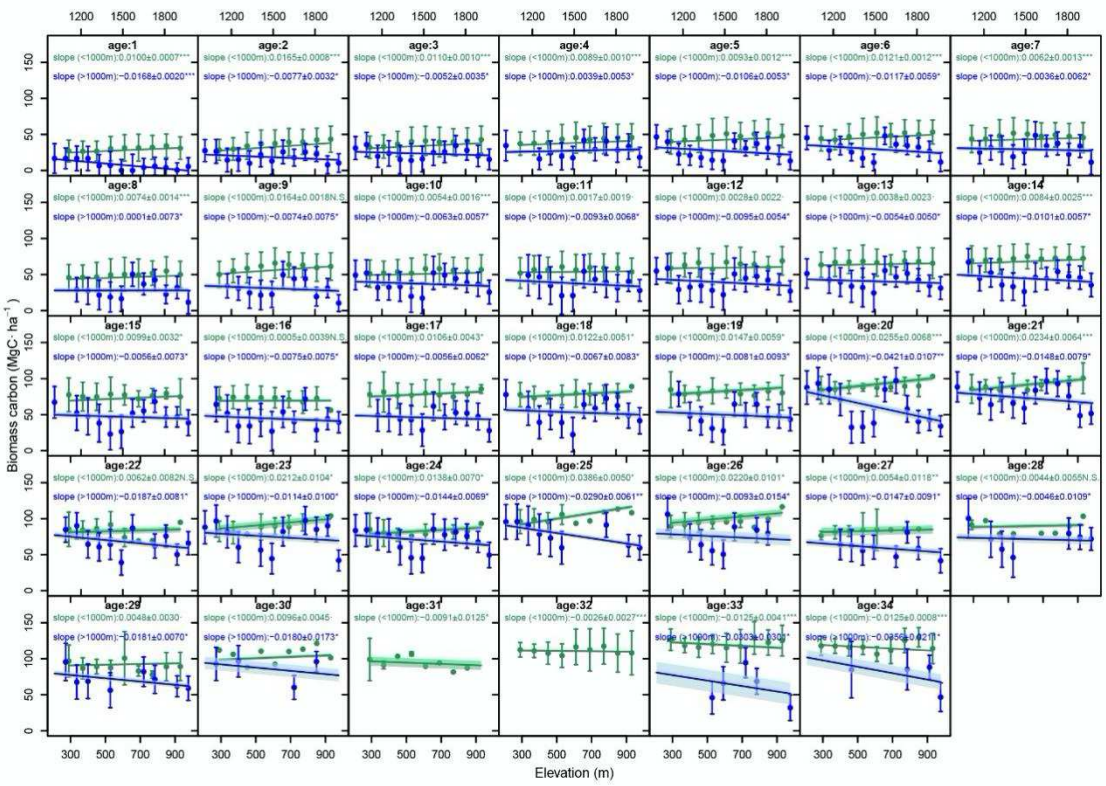

58

59 **Figure S6. The elevational patterns of ESA-CCI-derived biomass carbon in TPRFs**
60 **with different stand age classes.** The dots represent the mean biomass carbon of all
61 TPRF grid cells at each 100 m elevation bin; while error bars represent the
62 corresponding one standard deviation. Green and blue curves represent the linear fitting
63 regressions between the biomass carbon accumulation and elevation for elevation from
64 300 to 1000 m and elevation from 1000 to 2000 m, respectively. Shading represents the
65 95% confidence interval. Significance of linear regression is indicated in the legend as:
66 • P<0.5, * P<0.1, ** P<0.01, and *** P<0.001.

67

68

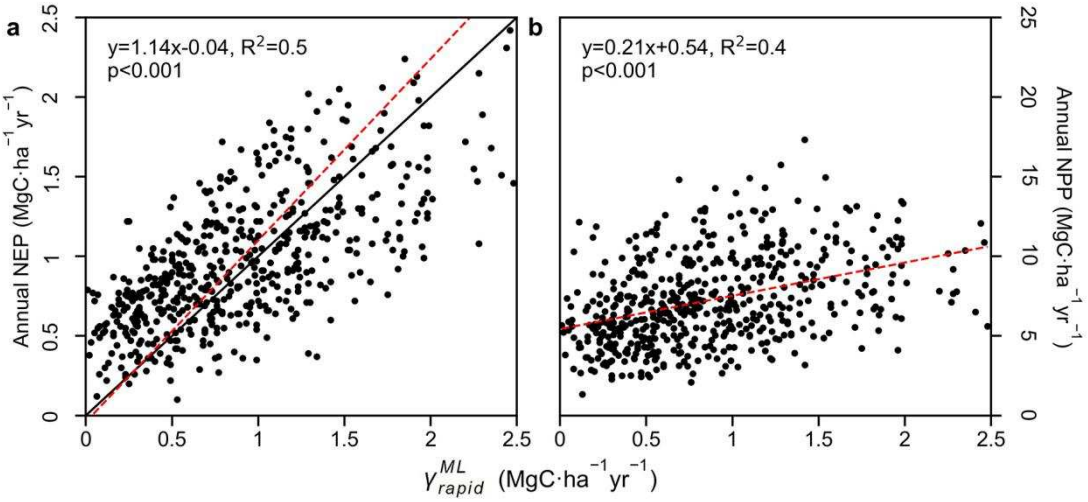

Figure S7. Correlation between annual BEPS-simulated NEP, NPP and γ_{rapid}^{ML} in TPRFs. a, Relationship between BEPS-simulated NEP and γ_{rapid}^{ML}. The magnitudes of NEP are similar as those of γ_{rapid}^{ML}. **b,** Relationship between NPP and γ_{rapid}^{ML}. The magnitudes of NPP are much larger than those of carbon γ_{rapid}^{ML}. The black dashed line is the 1:1 line.

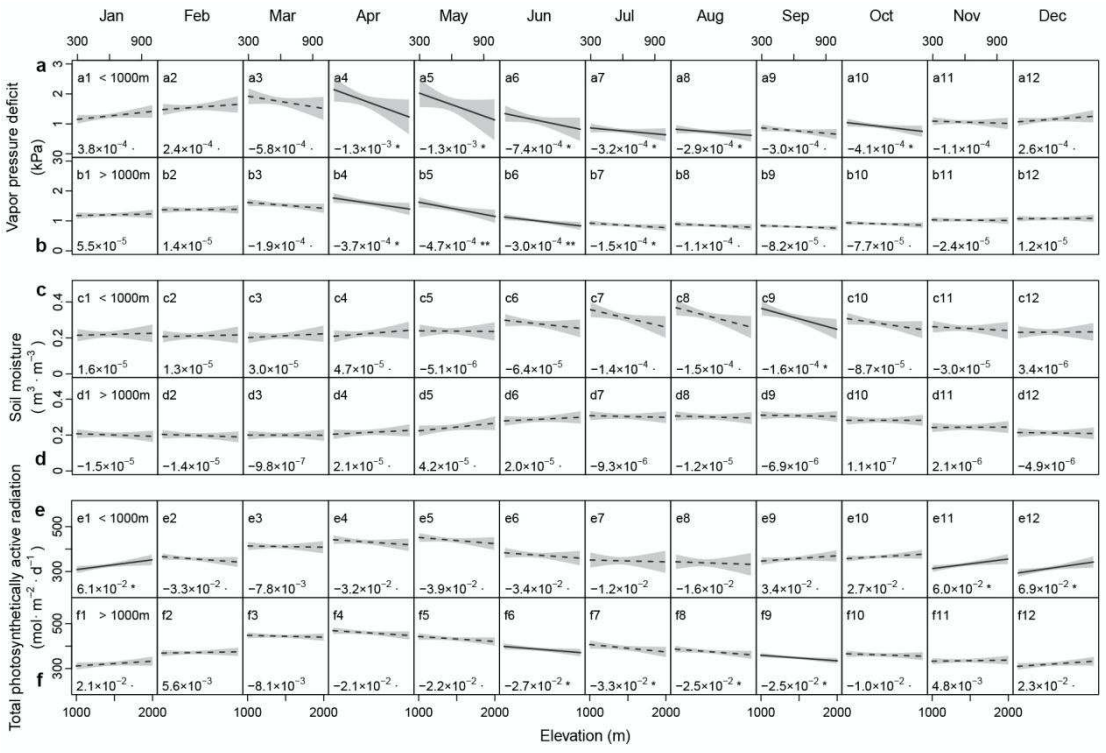

Figure S8. Elevational patterns of seasonal climate factors in TPRFs.

Linear regressions between monthly VPD (**a-b**), soil moisture (SM) (**c-d**) or total photosynthetically active radiation (Total PAR) (**e-f**) and elevation for range of 300-1000 m (**a, c, e**) and 1000-2000 m (**b, d, f**), respectively. Shadings indicate 95% confidence intervals. Significant relationships ($P \leq 0.05$) are shown in solid lines, and non-significant relationships ($P > 0.05$) in dashed lines. Significance of linear regression is indicated in the legend as: • $P < 0.5$, * $P < 0.1$, ** $P < 0.01$, and *** $P < 0.001$.

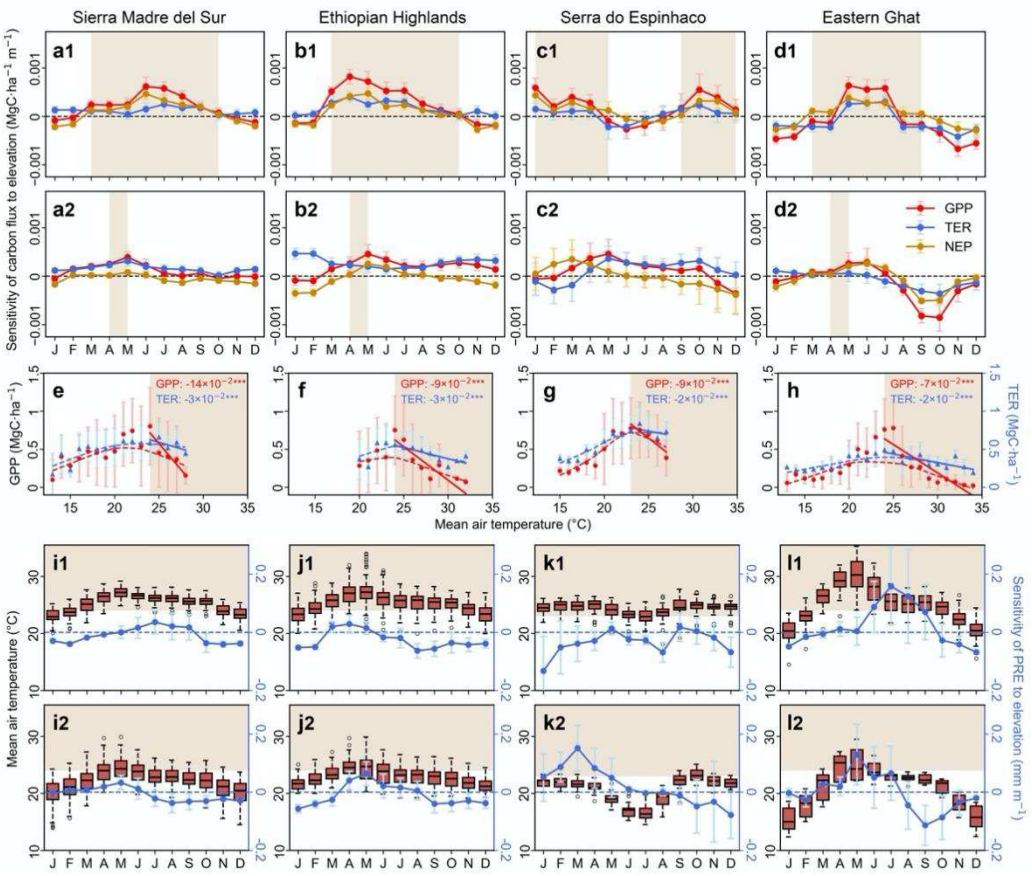

Figure S9. Sensitivity of carbon fluxes to elevation and the climatic driving mechanisms in four individual mountains. a-d, Seasonality of elevational sensitivity of GPP (red), TER (blue), NEP (orange) simulated by the BEPS model (**Dataset 4**) [30] for elevations between 300 and 1000 m (**a1-d1**) and for elevations between 1000 and 2000 m (**a2-d2**) in four individual mountains. Error bars represent one standard error. **e-h**, Changes in monthly GPP and TER with MAT in four individual mountains. Each dot denotes the median value of GPP (red) (or TER [blue]) within a 1°C MAT bin and error bars depict one standard deviation. The asterisks indicate the *P* values: **P*<0.05, ***P* < 0.01, and ****P* < 0.001. **i-l,** Seasonality of MAT and elevational sensitivity of TER for elevations between 300 and 1000 m (**i1-l1**) and for elevations between 1000 and 2000 m (**i2-l2**) in four individual mountains. The upper, center, and bottomed lines in the brown boxplot indicate the first, median, and third quartiles of monthly MAT. The blue points indicate the slope of linear regressions between PRE and elevation. Error bars represent one standard error.

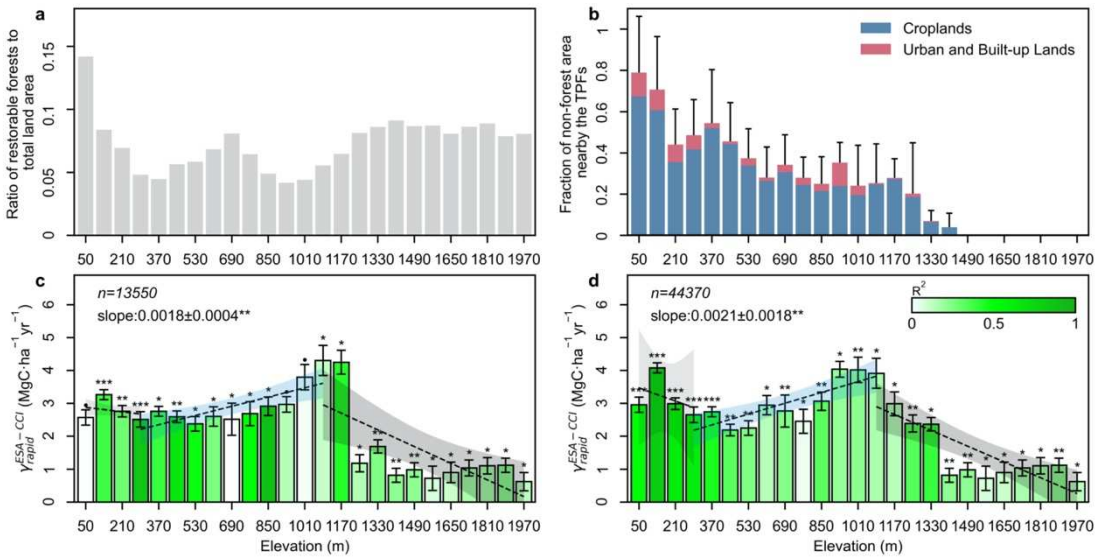

Figure S10. Land use characteristics and potential influences on the elevational pattern of $\gamma_{rapid}^{ESA-CCI}$ in TPRFs. a, The ratio of restorable forests to total land area for different elevation bin. The reforestation potential data was extracted from a global reforestation potential mapproposed by Griscom et al.[5], while the total land area was calculated from MODIS MCD12C1 landcover products[6]. **b**, The fraction of non-forest lands (urban and croplands) nearby the TPFs (neighbouring 10×10 1 km resolution pixels), calculated based on MODIS MCD12C1 landcover products[6]. **c**, The elevation patterns of $\gamma_{rapid}^{ESA-CCI}$ in TPRFs where their nearby fractions of non-forest lands are > 0.5%. **d**, The elevation patterns of $\gamma_{rapid}^{ESA-CCI}$ in TPRFs where their nearby fractions of non-forest lands are < 0.5%.

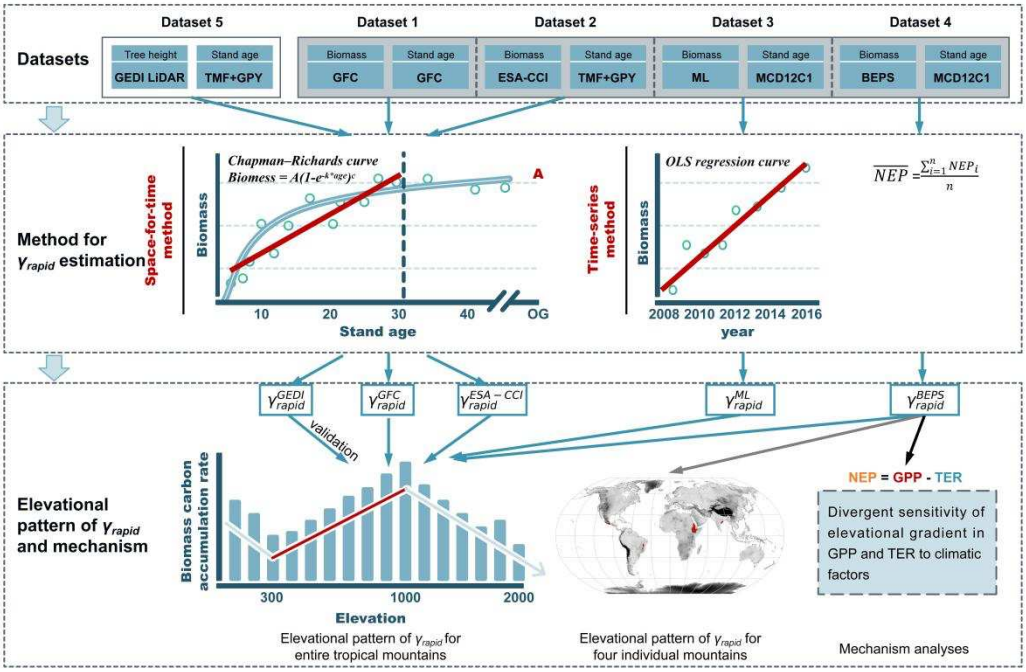

Figure S11. The flowchart illustrating the steps for analyzing the elevational pattern of γ_{rapid} and its underlying mechanisms.

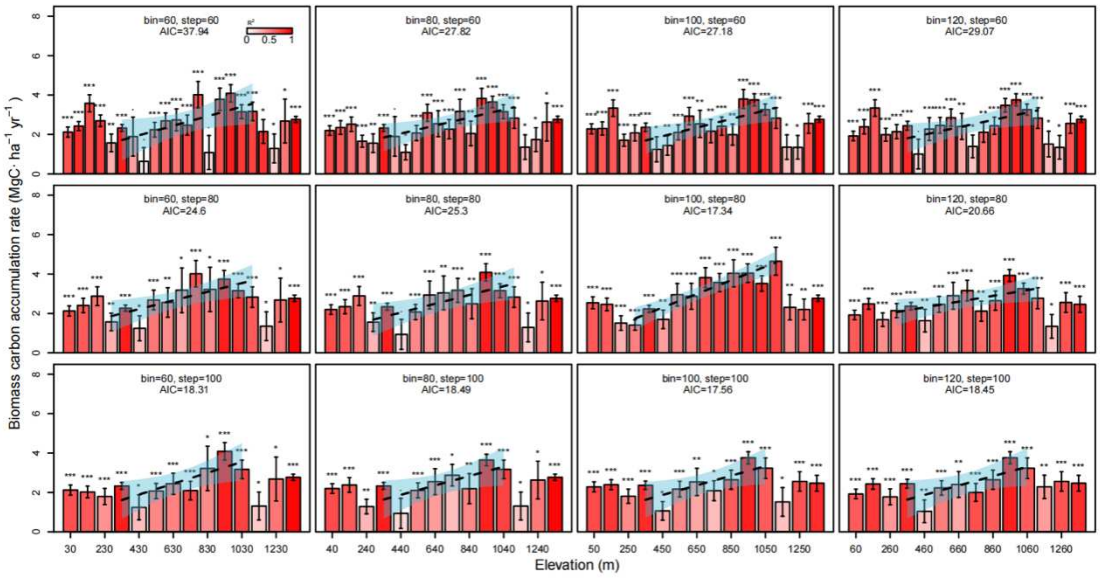

Figure S12. The elevation patterns of γ_{rapid}^{GFC} in TPRFs using various combinations of elevation bin and step settings. Each histogram represents the slope of the corresponding ordinary least squares regression (OLS) curve between *in situ* tree biomass of all sites of TPFs during the rapid growth stage of trees before approaching maturity (80% of the maximum biomass carbon) within the given elevation bin and moving step, using the space-for-time analogy method. R^2 of OLS regression is shown in a light-dark color gradient. Significance of OLS regression is indicated in the legend as: • $P<0.5$, *$P<0.1$, **$P<0.01$, and ***$P<0.001$. The error bars indicate one standard error of the estimated carbon accumulation rates. The dotted lines with shading represent the linear fitting curves between plant carbon accumulation rates and elevation with 95% confidence interval. Significant relationships ($P\leq0.05$) are shown in blue shading color while insignificant ones ($P>0.05$) are displayed in grey shading.

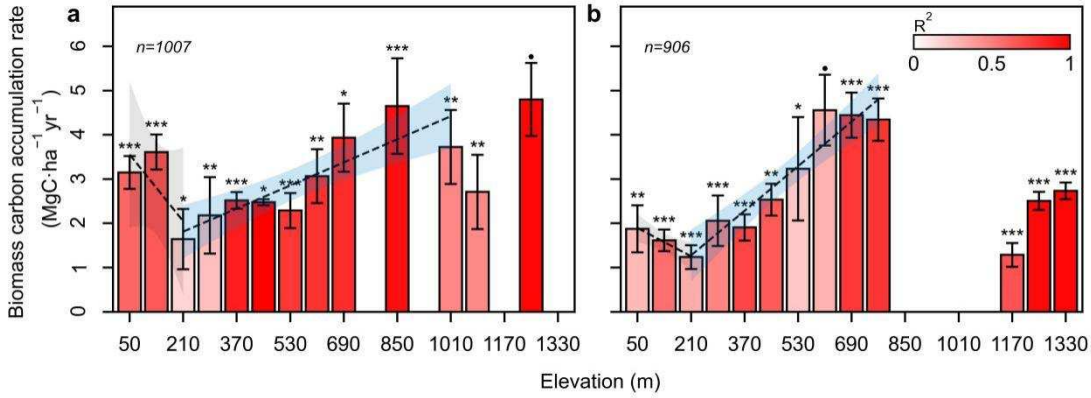

Figure S13. The elevation patterns of γ_{rapid}^{GFC} in TPRFs which used to be different land use types before afforestation. a, The elevation patterns of γ_{rapid}^{GFC} in TPRFs where were pasture lands before afforestation. **b,** The elevation γ_{rapid}^{GFC} in TPRFs where were shifting cultivation before afforestation. Each histogram represents the slope of the corresponding ordinary least squares regression (OLS) curve between *in situ* tree biomass of all sites of TPFs during the rapid growth stage of trees before approaching maturity (80% of the maximum biomass carbon) within each elevation bin (100±50m in 80m step) using the space-for-time analogy method. R^2 of OLS regression is shown in a light-dark color gradient. Significance of OLS regression is indicated in the legend as: • P<0.5, *P<0.1, **P<0.01, and ***P<0.001. The error bars indicate one standard error of the estimated carbon accumulation rates. The dashed lines with shading represent the linear fitting curves between plant carbon accumulation rates and elevation with 95% confidence interval. Significant relationships (P≤0.05) are shown in blue shading color while insignificant ones (P>0.05) are displayed in grey shading.

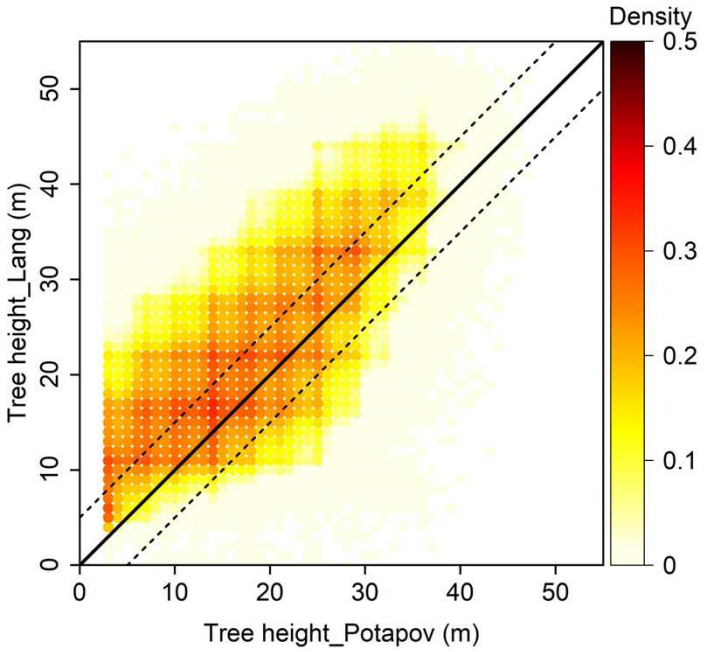

Figure S14. Selection of robust tree height data for estimating the tree height growth rate. We only selected those pixels where Potapov et al. (2021)'s[3] and Lang et al. (2023)'s[7] tree height data are highly consistent (±5 m) (**Methods**).

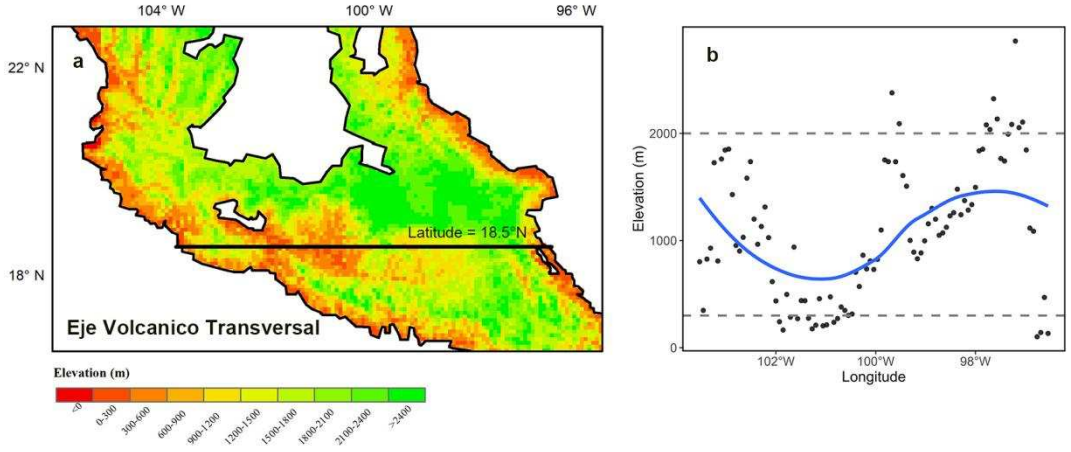

154

155 **Figure S15. Topography variations (10 km resolution) of the Eje Volcanico**
156 **Transversal mountain range in North America. a**, DEM map at a 10 km resolution.
157 **b,** Elevation data along the black line (Latitude:18.5°N; Longitude: 104°W ~ 96°W) on
158 the DEM map extracted from this 10 km resolution DEM for Eje Volcanico Transversal
159 mountain range.

160

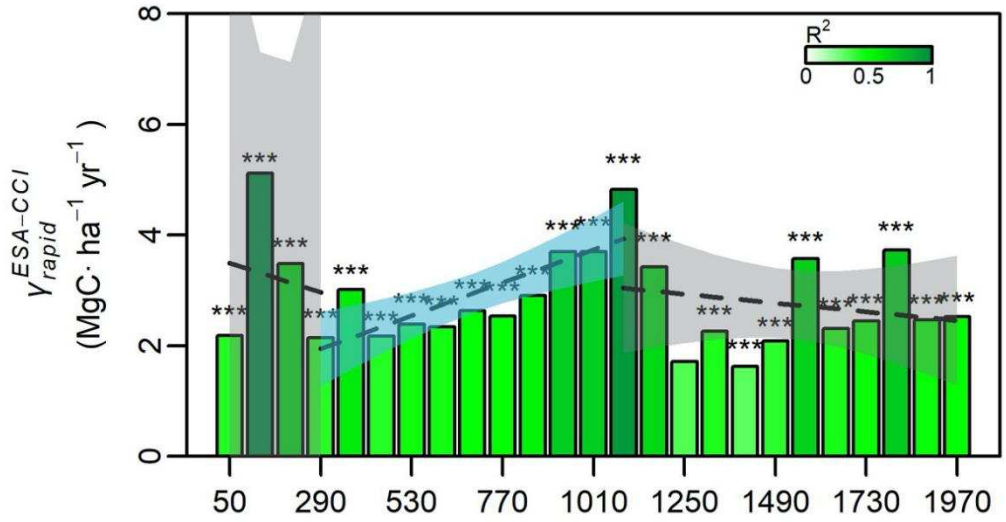

Figure S16. The elevation patterns of biomass carbon accumulation rates in TPFs based on adjusted ESA-CCI data. Each histogram represents the slope of corresponding ordinary least squares regression (OLS) curve between satellite-based tree biomass carbon and stand age of all pixels of TPFs within the given elevation bin (100±50 m in 80 m step), using the space-for-time analogy method (**Methods**). R^2 of OLS regression are shown in a light-dark color gradient. The error bars indicate one standard error. Significance of OLS regression is indicated in the legend as: • P<0.5, *P<0.1, **P<0.01, and ***P<0.001. The error bars indicate one standard error of the estimated carbon accumulation rates. The dashed lines with shading represent the linear fitting curves between plant carbon accumulation rates and elevation with 95% confidence interval. Significant relationships (P≤0.05) are shown in blue shading color while insignificant ones (P>0.05) are displayed in grey shading.

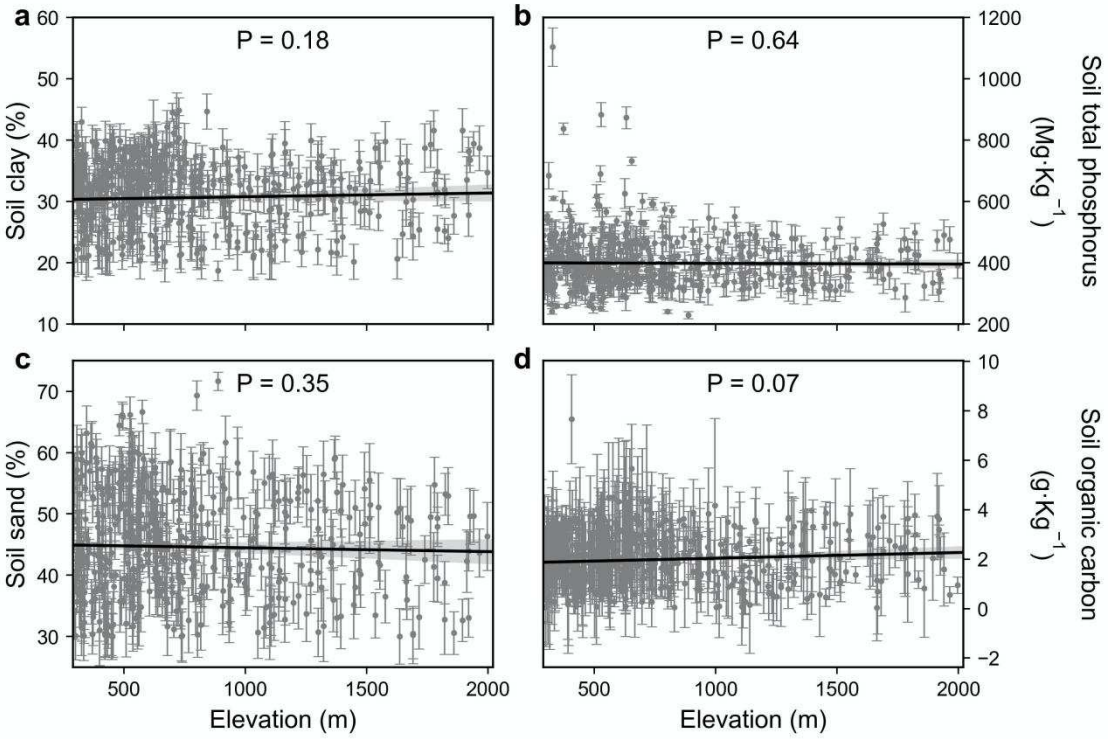

Figure S17. The elevation patterns of soil fertility in TPRFs. The elevation patterns of soil organic carbon[8], total phosphorus[9], sand[10] and clay[11] concentrations, respectively. Each dot represents the mean values of corresponding soil nutrient concentration of all soil layers at each TPRF site. Error bars represent one standard error. The solid lines represent the linear fitting curves between soil fertility and elevation. Shading represents the 95% confidence interval.

185 **Table S1.** Information on the data used in this study.

Name	Parameters	Spatial resolution	Temporal resolution	Reference	Applications
Field observation sites	Plant carbon, stand age and disturbance type	Multiple	Multiple	Cook-Patton et al., 2020[4], Anderson-Teixeira et al., 2018[12]	To calculate carbon accumulation rate
ESA-CCI forest above-ground biomass product	AGB	100 m	Yearly	Santoro & Cartus, 2021[13]	To extract forest AGB
Global vegetation live biomass	AGB	0.1°	Yearly	Xu et al., 2021[14]	To extract forest AGB
MCD12C1 v061	Land Cover	0.05°	Yearly	Friedl & Sulla-Menashe, 2022[6]	To identify forest regrowth period
Terra Climate	MAT, VPD, PRE and SM	1/24°, ~4-km	Monthly	Abatzoglou et al., 2018[15]	To extract environmental variables
BESS PAR	Total PAR	5km	Daily	Ryu et al., 2018[16]	To extract total PAR variable
Global remote-sensing-based surface soil moisture (RSSSM) dataset	Surface soil moisture	0.1°, ~ 10 km	~10 days	Chen et al., 2021[17]	To extract soil moisture variable
Global carbon flux	GPP, TER,	0.07272727	Daily	Chen et al.,	To extract

(GPP/NPP/NEP) simulation product	NEP and NPP	° ~10 km		2019[18]	carbon flux variables
Tropical moist forests	forest cover change	30 m	Yearly	Vancutsem et al., 2021[19]	To calculate forest age
FLUXCOM data	NEP	0.5°	Yearly	Jung et al., 2017[1]	To extract NEP
Tree height	tree height	10m	_	Lang et al., 2023[7]	To extract tree height
Tree height	tree height	30m	-	Potapov et al., 2021[3]	To extract tree height
Global reforestation potential map	reforestation potential	1km		Griscom et al., 2017[5]	To extract reforestation potential area
Global soil total phosphorus concentration dataset	total phosphorus	0.05°	-	He et al., 2021[9]	To extract soil fertility variables
Global soil organic carbon dataset	soil organic carbon	250m	-	Hengl & Wheeler. 2018[8]	To extract soil fertility variables
Global soil sandy content dataset	soil sandy concentratio ns	250m	-	Hengl et al., 2018[10]	To extract soil fertility variables
Global soil clay content dataset	soil clay concentratio ns	250m	-	Hengl et al., 2018[11]	To extract soil fertility variables
RAINBIO mega database	tree species	Multiple	Multiple	Dauby et al., 2016[2]	To extract tree species information

	SRTM DEM	elevation	30m	-	Van Zyl et al., 2001[20]	To extract elevation

186

187

188

References:

1. Jung, M., Reichstein, M., Schwalm, C. R., Huntingford, C., Sitch, S., Ahlström, A., Arneth, A., Camps-Valls, G., Ciais, P., Friedlingstein, P., Gans, F., Ichii, K., Jain, A. K., Kato, E., Papale, D., Poulter, B., Raduly, B., Rödenbeck, C., Tramontana, G., Viovy, N., Wang, Y.-P., Weber, U., Zaehle, S. n., & Zeng, N. 2017. Compensatory water effects link yearly global land CO_2 sink changes to temperature. Nature, 541(7638): 516-520.
2. Dauby, G., Zaiss, R., Blach-Overgaard, A., Catarino, L., Damen, T., Deblauwe, V., Dessein, S., Dransfield, J., Droissart, V., Duarte, M. C., Engledow, H., Fadeur, G., Figueira, R., Gereau, R. E., Hardy, O. J., Harris, D. J., de Heij, J., Janssens, S., Klomberg, Y., Ley, A. C., Mackinder, B. A., Meerts, P., van de Poel, J. L., Sonké B, B., Sosef, M. S., Stévart, T., Stoffelen, P., Svenning, J. C., Sepulchre, P., van der Burgt, X., Wieringa, J. J., & Couvreur, T. L. 2016. RAINBIO: A mega-database of tropical African vascular plants distributions. PhytoKeys, (74), 1.
3. Potapov, P., Li, X., Hernandez-Serna, A., Tyukavina, A., Hansen, M. C., Kommareddy, A., Pickens, A., Turubanova, S., Tang, H., Silva, C. E., Armston, J., Dubayah, R., Blair, J. B., & Hofton, M. 2021. Mapping global forest canopy height through integration of GEDI and landsat data. Remote Sensing of Environment, 253: 112165.
4. Cook-Patton, S. C., Leavitt, S. M., Gibbs, D., Harris, N. L., Lister, K., Anderson-Teixeira, K. J., Briggs, R. D., Chazdon, R. L., Crowther, T. W., Ellis, P. W., Griscom, H. P., Herrmann, V., Holl, K. D., Houghton, R. A., Larrosa, C., Lomax, G., Lucas, R., Madsen, P., Malhi, Y., Paquette, A., Parker, J. D., Paul, K., Routh, D., Roxburgh, S., Saatchi, S., van den Hoogen, J., Walker, W. S., Wheeler, C. E., Wood, S. A., Xu, L., & Griscom, B. W. 2020. Mapping carbon accumulation potential from global natural forest regrowth. Nature, 585(7826): 545-550.
5. Griscom, B.W., Adams, J., Ellis, P.W., Houghton, R.A., Lomax, G., Miteva, D.A., Schlesinger, W.H., Shoch, D., Siikamäki, J.V., Smith, P. and Woodbury, P., 2017. Natural climate solutions. Proceedings of the National Academy of Sciences, 114(44), pp.11645-11650.

6. Friedl, M. & Sulla-Menashe, D. MODIS/Terra+Aqua Land Cover Type Yearly L3 Global 0.05Deg CMG V061 [Data set] (NASA EOSDIS Land Processes DAAC, 2022); https://doi.org/10.5067/MODIS/MCD12C1.061.
7. Lang, N., Jetz, W., Schindler, K., & Wegner, J. D. 2023. A high-resolution canopy height model of the earth. Nature Ecology & Evolution: 1-12.
8. Hengl, T & Wheeler, I. 2018. Soil organic carbon content in x 5 g / kg at 6 standard depths (0, 10, 30, 60, 100 and 200 cm) at 250 m resolution (v0.2). Zenodo. https://doi.org/10.5281/zenodo.2525553.
9. He, X., Augusto, L., Goll, D. S., Ringeval, B., Wang, Y., Helfenstein, J., Huang, Y., Yu, K., Wang, Z., Yang, Y., & Hou, E. 2021. Global patterns and drivers of soil total phosphorus concentration. Earth Syst. Sci. Data, 13(12): 5831-5846. http://dx.doi.org/10.5285/84403d09cef3485883158f4df2989b0c.
10. Hengl, T. 2018. Sand content in % (kg / kg) at 6 standard depths (0, 10, 30, 60, 100 and 200 cm) at 250 m resolution (v0.2). Zenodo. https://doi.org/10.5281/zenodo.2525662.
11. Hengl, T. 2018. Clay content in% (kg / kg) at 6 standard depths (0, 10, 30, 60, 100 and 200 cm) at 250 m resolution. Zenodo. https://zenodo.org/records/2525663.
12. Anderson-Teixeira, K. J., Wang, M. M., McGarvey, J. C., Herrmann, V., Tepley, A. J., Bond-Lamberty, B., & LeBauer, D. S. 2018. ForC: A global database of forest carbon stocks and fluxes. Ecology, 99(6): 1507.
13. Santoro, M., Cartus, O. 2021. ESA Biomass Climate Change Initiative (Biomass_CCI): Global datasets of forest above-ground biomass for the years 2010, 2017 and 2018, v2. Centre for Environmental Data Analysis.
14. Xu, L., Saatchi, S. S., Yang, Y., Yu, Y., Pongratz, J., Bloom, A. A., Bowman, K., Worden, J., Liu, J., Yin, Y., Domke, G., McRoberts, R. E., Woodall, C., Nabuurs, G.-J., de-Miguel, S., Keller, M., Harris, N., Maxwell, S., & Schimel, D. Changes in global terrestrial live biomass over the 21st century. Science Advances, 7(27): eabe9829.
15. Abatzoglou, J. T., Dobrowski, S. Z., Parks, S. A., & Hegewisch, K. C. 2018. Terraclimate, a high-resolution global dataset of monthly climate and climatic

water balance from 1958-2015. Scientific Data, 5(1): 170191.

16. Ryu, Y., Jiang, C., Kobayashi, H., & Detto, M. 2018. Modis-derived global land products of shortwave radiation and diffuse and total photosynthetically active radiation at 5 km resolution from 2000. Remote Sensing of Environment, 204: 812-825.
17. Chen,Y., Feng, X., & Fu, B. 2021. An improved global remote-sensing-based surface soil moisture (RSSSM) dataset covering 2003–2018. Earth System Science Data, 13(1): 1-31.
18. Chen, J. M., Ju, W., Ciais, P., Viovy, N., Liu, R., Liu, Y., & Lu, X. 2019. Vegetation structural change since 1981 significantly enhanced the terrestrial carbon sink. Nature Communications, 10(1): 4259.
19. Vancutsem, C., Achard, F., Pekel, J. F., Vieilledent, G., Carboni, S., Simonetti, D., Gallego, J., Aragao, L. E. O. C., & Nasi, R. 2021. Long-term (1990-2019) monitoring of forest cover changes in the humid tropics. Science Advances, 7(10): eabe1603.
20. Van Zyl, J. J. 2001. The Shuttle Radar Topography Mission (SRTM): A breakthrough in remote sensing of topography. Acta astronautica, 48(5-12): 559-565.
21. Abrams, M., Crippen, R., & Fujisada, H. 2020. Aster global digital elevation model (GDEM) and aster global water body dataset (ASTWBD). Remote Sensing, 12(7): 1156.
22. Tadono, T., Nagai, H., Ishida, H., Oda, F., Naito, S., Minakawa, K., & Iwamoto, H. 2016. Generation of the 30 m-mesh global digital surface model by ALOS PRISM. The international archives of the photogrammetry, remote sensing and spatial information sciences, 41: 157-162.